

Journal of Geophysical Research: Planets

RESEARCH ARTICLE

10.1002/2014JE004714

Key Points:

- New core cracking model coupled to a thermal evolution code
- Enough fractured rock on Ceres for hydrothermal interaction
- Hydrothermal circulation can profoundly affect Ceres' evolution

Correspondence to:M. Neveu,
mneveu@asu.edu**Citation:**

Neveu, M., S. J. Desch, and J. C. Castillo-Rogez (2015), Core cracking and hydrothermal circulation can profoundly affect Ceres' geophysical evolution, *J. Geophys. Res. Planets*, 120, doi:10.1002/2014JE004714.

Received 18 AUG 2014

Accepted 20 DEC 2014

Accepted article online 29 DEC 2014

Core cracking and hydrothermal circulation can profoundly affect Ceres' geophysical evolution

Marc Neveu¹, Steven J. Desch¹, and Julie C. Castillo-Rogez²

¹School of Earth and Space Exploration, Arizona State University, Tempe, Arizona, USA, ²Jet Propulsion Laboratory, California Institute of Technology, Pasadena, California, USA

Abstract Observations and models of Ceres suggest that its evolution was shaped by interactions between liquid water and silicate rock. Hydrothermal processes in a heated core require both fractured rock and liquid. Using a new core cracking model coupled to a thermal evolution code, we find volumes of fractured rock always large enough for significant interaction to occur. Therefore, liquid persistence is key. It is favored by antifreezes such as ammonia, by silicate dehydration which releases liquid, and by hydrothermal circulation itself, which enhances heat transport into the hydrosphere. The effect of heating from silicate hydration seems minor. Hydrothermal circulation can profoundly affect Ceres' evolution: it prevents core dehydration via "temperature resets," core cooling events lasting ~50 Myr during which Ceres' interior temperature profile becomes very shallow and its hydrosphere is largely liquid. Whether Ceres has experienced such extensive hydrothermalism may be determined through examination of its present-day structure. A large, fully hydrated core (radius 420 km) would suggest that extensive hydrothermal circulation prevented core dehydration. A small, dry core (radius 350 km) suggests early dehydration from short-lived radionuclides, with shallow hydrothermalism at best. Intermediate structures with a partially dehydrated core seem ambiguous, compatible both with late partial dehydration without hydrothermal circulation, and with early dehydration with extensive hydrothermal circulation. Thus, gravity measurements by the *Dawn* orbiter, whose arrival at Ceres is imminent, could help discriminate between scenarios for Ceres' evolution.

1. Introduction

The imminent exploration by spacecraft of the dwarf planet Ceres has motivated recent extensive telescopic observations [Thomas *et al.*, 2005; Li *et al.*, 2006; Carry *et al.*, 2008; Drummond and Christou, 2008; Milliken and Rivkin, 2009; Rousselot *et al.*, 2011; Küppers *et al.*, 2014; Drummond *et al.*, 2014], as well as the development of models of Ceres' geophysical evolution and present state [McCord and Sotin, 2005; Castillo-Rogez and McCord, 2010; Castillo-Rogez *et al.*, 2007; Zolotov, 2014]. Observations and models both suggest that liquid water may have persisted in the interior of Ceres over geological timescales, possibly until present [Castillo-Rogez and McCord, 2010; Rivkin *et al.*, 2011; McCord *et al.*, 2012]. Liquid persistence may be enabled below 273 K by salt or volatile antifreezes such as methanol or ammonia [Hussmann *et al.*, 2006; Desch *et al.*, 2009; Castillo-Rogez and McCord, 2010; Sohl *et al.*, 2010].

If present over such extended timescales, liquid water could have played a major role in shaping the geophysical evolution of Ceres. For example, interactions between liquid water and Ceres' rocky core could have occurred, altering physical and chemical properties of the silicates. Common products of such interactions, carbonates, and clay minerals are seen on Ceres' surface [Milliken and Rivkin, 2009; Rivkin *et al.*, 2011]. Water-rock interactions may have influenced Ceres' geophysical evolution in several ways. First, dry silicates may have hydrated once in contact with liquid water at lower temperatures. Hydration causes rock to swell and tends to decrease its thermal conductivity [Horai, 1971; Castillo-Rogez and McCord, 2010], resulting in a larger core that better retains heat. Second, hydration reactions tend to be highly exothermic [Cohen and Coker, 2000], adding to Ceres' heat budget. Third, chemical interactions between water and rock may leach out radiogenic elements, such as potassium, from core silicates [Castillo-Rogez and Lunine, 2010; Castillo-Rogez and McCord, 2010]. Similarly, salt or volatile antifreezes such as ammonia, invoked as a requirement for liquid over the long term [e.g., Desch *et al.*, 2009; Castillo-Rogez and McCord, 2010; Rubin *et al.*, 2014], may be produced or consumed in water-rock reactions [Matson *et al.*, 2007; Fortes *et al.*, 2007; Glein *et al.*, 2009]. Finally, water can circulate through pores or fractures in the core and efficiently transport heat outward in a convective pattern known as hydrothermal circulation [Young, 2001; Young *et al.*, 2003].

The major part of water-rock interactions presumably occurs in core macrofractures and microfractures (connected pores), because these offer a much greater area of water-rock interface than the core's outer surface ("seafloor"), as well as higher temperatures that speed up kinetically controlled chemical reactions. Moreover, core fractures could feature chemical disequilibria at water-rock interfaces. The availability of chemical energy and presence of liquid water make long-lived core cracks a potential habitat for life as we know it.

The extent of fracturing in Ceres' core is unknown, and, to our knowledge, neither the extent of core fracturing nor the effects of water-rock interaction have been investigated in models of Ceres' evolution. A key reason for this is that models of core fractures on icy bodies have focused on cooling cracks [Vance *et al.*, 2007], while models of Ceres suggest that by the time the core starts cooling, the icy shell is mostly frozen [Castillo-Rogez and McCord, 2010]. However, the problem is still worth visiting, first because long-term liquid may persist due to antifreezes, and second because cracking can also result from heating [Norton, 1984], which on Ceres likely occurred concurrently with the presence of liquid [Castillo-Rogez and McCord, 2010].

Coupled geophysical-geochemical evolution models have so far focused on the evolution of planetesimals [Cohen and Coker, 2000; Grimm and McSween, 1989; Palguta *et al.*, 2010] or icy moons [Travis *et al.*, 2012]. Local hydrothermal systems around magmatic intrusions on Martian volcanoes or impact craters have also been modeled [e.g., Newsom, 1980; Gulick, 1998; Rathbun and Squyres, 2002; Abramov and Kring, 2005; Pope *et al.*, 2006; Barnhart *et al.*, 2010; Schwenzer *et al.*, 2012]. Several of these studies have used numerical codes developed for Earth applications, such as SUTRA [Voss and Provost, 2010] and HYDROTHERM [Hayba and Ingebritsen, 1994], which model fluid flow in porous media. A third code, MAGHNUM, was developed to model local hydrothermal systems on planets [Travis *et al.*, 2003], and later expanded as a global planetary thermal evolution code [e.g., Travis *et al.*, 2012]. Although MAGHNUM incorporates the effects of hydrothermal circulation, it does not account for silicate hydration or dehydration. A geophysical model of the present state of potential hydrothermal systems on water-rich bodies has been developed [Vance *et al.*, 2007; Sohl *et al.*, 2010], but this model has not been applied to Ceres and neglects time evolution. This model is further discussed below. Finally, time-evolution models developed by Malamud and Prialnik [2013, 2015] and applied to Enceladus, Mimas, and Kuiper belt objects include the rock swelling and heating effects due to serpentinization, the flow of water liquid and vapor, and a detailed treatment of rock and ice porosity by means of equations of state. These models therefore offer an opportunity for comparison with those presented here.

There exist recent, sophisticated models of hydrothermal systems in the Earth sciences. These generally focus on a specific aspect of these systems, such as 3-D fluid flow in porous or fractured media [Person *et al.*, 2012], vapor-brine phase separation and salinity [Han *et al.*, 2013], or transport of reactive fluid [Steele-MacInnis *et al.*, 2012; Ord *et al.*, 2012]. In practice, these aspects feed back on one another. However, their integration into a single detailed model of the physics and chemistry of local or globally averaged hydrothermal systems remains a challenge to existing computational capabilities [Ingebritsen and Appold, 2012]. Most of these models do not discuss the appearance or disappearance of pores or fractures, not only mainly because the feedbacks with reactive hydrothermal flow are not well understood [Ingebritsen *et al.*, 2010] but also because many models focus on simulating hydrothermal systems limited in their spatial extent and lifetime. The models that focus on spatially variable or anisotropic porosity and permeability generally assume that these properties remain invariant over time [Xu and Pruess, 2001; Jones *et al.*, 2004], or consider simple geometries of restricted spatial extent [Bolton *et al.*, 1999].

In the following sections, we first briefly review the global thermal evolution model on which we base this study [Desch *et al.*, 2009]. Next, we present a model for core fracturing which expands on the work of Vance *et al.* [2007] and suggestions of Travis *et al.* [2012], and which is inspired by models of hydrothermal systems on Earth. We then explain how this model is incorporated as a cracking subroutine into the thermal evolution code of Desch *et al.* [2009], along with the inclusion of silicate hydration and dehydration, and hydrothermal circulation in the porous layer. The level of detail in the resulting code is similar to that of Malamud and Prialnik [2013, 2015], albeit with a different approach in the treatment of differentiation, porosity, and hydrothermal heat transfer. We apply the model to Ceres and investigate the influence of fracturing and physical water-rock processes on its evolution.

2. Thermal Evolution Code

The code of *Desch et al.* [2009] performs time-dependent calculations of the internal temperature profile and structure of bodies made of rock and ice. It is applicable to objects roughly 300 to 1500 km in radius, as it neglects porosity (significant below this radius range) and the compressibility of rocky and icy materials (significant above this range) as well as high-pressure phases of ice.

Inputs to the code are body radius, density, ammonia content, surface temperature, initial temperature (isothermal radial profile), and time of formation, as well as the total simulation time. From the density input, a bulk rock-to-ice ratio is determined. The initial structure is assumed homogeneous and undifferentiated, and mass is distributed assuming spherical symmetry on a fixed-volume 1-D grid, with a specified number of zones evenly distributed in radius (typically 200). The internal energy in each grid zone is computed from the initial temperature using equations of state, detailed by *Desch et al.* [2009], for rock and ice (which includes water ice I, liquid water, liquid ammonia, and ammonia dihydrate I). It is assumed that any accretional heating has been dissipated before the starting time of the simulation.

From this initial state, the internal energy E_i in each grid zone i of outer radius r_i is updated after a time step Δt . This time step (typically fixed at 50 years) must satisfy a Courant condition $\Delta t < \min[(\Delta r)^2/(2\kappa_d)]$, where κ_d is the thermal diffusivity. Energy changes are due to heat fluxes F_i out of each zone, radiogenic heating $Q_{i,\text{rad}}$, and gravitational energy release $Q_{i,\text{grav}}$:

$$\frac{E_i(t + \Delta t) - E_i(t)}{\Delta t} = 4\pi r_{i-1}^2 F_{i-1} - 4\pi r_i^2 F_i + Q_{i,\text{rad}}(t) + Q_{i,\text{grav}} \quad (1)$$

Heat fluxes, assumed conductive, are computed using a finite-difference scheme as follows:

$$F_i = -\frac{k_i + k_{i+1}}{2} \frac{T_{i+1} - T_i}{(r_{i+1} - r_{i-1})/2} \quad (2)$$

Here k_i are the thermal conductivities in each grid zone; chosen expressions are given by *Desch et al.* [2009] and in Table 4. In the ice shell, possible heat transfer by solid-state convection, rather than conduction, is accounted for by parameterizing k_i in terms of the Rayleigh number in the shell [*Desch et al.*, 2009]. Vigorous convective heat transfer is also assumed to occur in any grid zone containing more than 2% liquid ("slush"); in this case the thermal conductivity is set arbitrarily to a value of $400 \text{ W m}^{-1} \text{ K}^{-1}$, high enough to obtain a near-isothermal temperature profile across the slush layer. T_i are the temperatures, computed such that E_i is the energy required to raise the mix of rock and ices from 0 K to T_i , including phase transitions, using the equations of state mentioned above. The boundary conditions are zero heat flux at the center (by symmetry), and a fixed temperature (i.e., fixed energy) at the surface as determined in the input.

The heating term $Q_{i,\text{rad}}(t)$ due to the decay of radionuclides j is given by

$$Q_{i,\text{rad}}(t) = M_{\text{rock},i} \sum_j N_j \Delta E_j \ln(2)/t_{1/2,j} \exp(-\ln(2)/t_{1/2,j} \times t) \quad (3)$$

where $M_{\text{rock},i}$ is the mass of silicate rock in a zone i , N_j is the number of atoms of the nuclide j per kg of rock, ΔE_j is the energy produced per decay, and $t_{1/2,j}$ is the nuclide half-life. These parameters are given by *Desch et al.* [2009] for the long-lived radionuclides ^{40}K , ^{232}Th , ^{235}U , and ^{238}U . ^{26}Al decay heating is also accounted for, assuming a half-life of 716,000 years, a $^{26}\text{Al}/^{27}\text{Al}$ atomic fraction of 5×10^{-5} [*Castillo-Rogez et al.*, 2010], an initial abundance of 8.41×10^4 Al atoms per 10^6 Si atoms [*Lodders*, 2003], and a calculated energy heat per decay ΔE of 3.177 MeV (within 2% of the value estimated by *Castillo-Rogez et al.* [2010] using the same method, but slightly different assumptions on neutrino energies [*Desch et al.*, 2009]). These values yield an initial heating rate $\Delta E_j(\ln 2/t_{1/2,j})(N_j/10^6)/(151 \text{ m}_{\text{nucleon}})$ of $0.26 \mu\text{W/kg}$ of rock, assuming that rock contains on average 151 nucleons for every Si atom.

Ice-rock differentiation occurs if the temperature in a zone exceeds a threshold T_{diff} . Physically, it is assumed that differentiation is initiated by ice melting at a temperature of first melt (solidus) that depends on initial ammonia content. For nonnegligible amounts of ammonia (arbitrary mass fraction of 10^{-2} with respect to H_2O), we set $T_{\text{diff}} = 176 \text{ K}$; otherwise, we set $T_{\text{diff}} = 273 \text{ K}$. In practice, melting first occurs in the central zones and differentiation proceeds outward. In all the zones exceeding T_{diff} , the code redistributes mass by first filling the innermost zones with rock, then the zones surrounding this rocky core

with liquids and ammonia dihydrate, and finally the outermost differentiated zones with pure water ice. This approach ensures mass conservation. Volume changes are precluded by choosing fixed densities for liquid water and ammonia, slightly different from their actual values: the density of liquid water $\rho_{\text{H}_2\text{O}(\text{l})}$ is equated to that of ice $\rho_{\text{H}_2\text{O}(\text{s})}$, and the density of ammonia $\rho_{\text{NH}_3(\text{l})}$ is determined by mass balance: $\rho_{\text{NH}_3(\text{l})}^{-1} = \rho_{\text{H}_2\text{O}(\text{l})}^{-1} + (\rho_{\text{H}_2\text{O}(\text{s})}^{-1} + \rho_{\text{ADH}(\text{s})}^{-1})/X_c$, where $\rho_{\text{ADH}(\text{s})}^{-1}$ is the density of ammonia dihydrate and $X_c = 0.321$ is the eutectic ammonia mass fraction. Density values are provided by *Desch et al.* [2009].

Differentiation leads to a gravitationally unstable configuration, with an ice mantle underneath a denser, undifferentiated crust. Such a configuration is prone to Rayleigh-Taylor instabilities, which *Rubin et al.* [2014] showed act on geological timescales in zones where $T_i > T_{\text{diff}} \approx 140$ K. This value of T_{diff} is adopted in the late stages of differentiation.

Differentiation generates heat due to gravitational energy release. The gravitational potential energy U_g is calculated at each time step:

$$U_g = -G \int_0^{R_p} 4\pi r^2 \rho(r) \frac{M(r)}{r} dr \quad (4)$$

where $M(r)$ is the mass enclosed within a sphere of radius r and G is the gravitational constant. If differentiation has redistributed mass and changed U_g during a time step, this energy difference ΔU_g is redeposited uniformly throughout all differentiated shells, out to a radius R_{diff} . The corresponding heating term $Q_{i,\text{grav}}$ in equation (1) is given by

$$Q_{i,\text{grav}} = \frac{\Delta U_g}{\Delta t} \frac{r_i^3 - r_{i-1}^3}{R_{\text{diff}}^3} \quad (5)$$

This thermal evolution code, which accounts for ice-rock differentiation and ammonia antifreeze, is our starting point for exploring consequences of the persistence of liquid water interacting with a rocky core over geological timescales. We now proceed to quantify the extent of these interactions using a core fracturing model, which we describe below.

3. Geophysical-Geochemical Model of Core Fracturing

Modeling the extent of macrofracturing and microfracturing in the cores of icy worlds over geologic time provides an estimate of the extent of hydrothermal circulation. In turn, such estimates constrain the magnitude of the coupling between geophysical and geochemical processes in icy world evolution. In this section, we describe a new model of core fracturing.

We assume that icy body cores are made of ferromagnesian silicate minerals, either dry or hydrated. Such compositions are typical of Earth's upper mantle [*Sohl et al.*, 2010], and also compose ordinary and carbonaceous chondrites. Therefore, we do not account for alkali-rich minerals.

We model five phenomena which may influence core fracturing on small and large scales: (1) the brittle-ductile transition in hydrated rock; microcracking by (2) thermal expansion mismatch of mineral grains and (3) expansion of pore water upon heating; and microcrack and macrocrack shrinking due to (4) rock swelling during hydration (as well as crack widening during dehydration) and (5) precipitation of mineral species (as well as widening due to dissolution). We account for elastic opening and closing of cracks. Many other phenomena may affect cracking, such as compaction and thermal expansion of the solid rock matrix [*Germanovich et al.*, 2001], increases in fluid pressures from precipitation clogging [*Germanovich et al.*, 2001], exsolution of volatiles from water [*Kelley et al.*, 1993], pressure solution of species [*Bolton et al.*, 1999], anisotropy in the permeability of rock [*Bolton et al.*, 1999], multiphase flows [*Goldfarb and Delaney, 1988; Xu and Pruess, 2001; Ingebritsen et al., 2010; Han et al., 2013*], and exogenous impacts [*Bowling et al., 2014*]. We neglect these phenomena in this simple approach.

3.1. Brittle-Ductile Transition in Hydrated Rock

The extent of core cracking is limited by the healing timescale of cracks. Cracks heal when rock accommodates stresses in a ductile or plastic fashion at high pressure and temperature. We do not distinguish between the brittle-ductile and brittle-plastic transitions [*Kohlstedt et al.*, 1995] and will refer to the transition as brittle-ductile. This transition occurs when the brittle and ductile rock strengths are equal.

Such a model successfully predicts the strength profile of Earth's lithosphere with depth [Kohlstedt *et al.*, 1995; Escartin *et al.*, 1997a].

The frictional strength of brittle rock, τ , is given as a function of normal stress σ by [e.g., Kohlstedt *et al.*, 1995]

$$\tau = \mu_f (\sigma - P_w) + C_f \quad (6)$$

where μ_f is the coefficient of friction, P_w is the fluid pressure, and C_f is the frictional cohesive strength. Empirically, μ_f and C_f are found to be similar regardless of rock type [Byerlee, 1978], leading to a relationship called Byerlee's rule: $\tau = 0.85 \sigma$ for $\sigma < 200$ MPa, and $\tau = 50 + 0.6\sigma$ between 200 and 1700 MPa ($C_f = 50$ has units of MPa). Hydrated clays are exceptions to this rule [Brace and Kohlstedt, 1980]: for serpentine rock (lizardite, antigorite, or chrysotile), Escartin *et al.* [1997b, 2001] found that a brittle strength with $\mu_f = 0.3$ to 0.5 and $C_f = 0$ better fitted data from deformation experiments at pressures up to 1 GPa. The dependence of μ_f on temperature is unclear, with reports of both increases [Moore *et al.*, 1997] and decreases within a large range of 0.1 to 0.85 [Hirth and Guillot, 2013]. Strengths $\tau \approx 0.4\sigma$ also seem to apply to rocks that are just slightly serpentized [Escartin *et al.*, 2001]. We adopt values of 0.4 for μ_f and set $C_f = 0$ for hydrated silicates, use Byerlee's rule for dry silicates, and combine linearly the dry and hydrated rock strengths for partially hydrated silicates. We neglect changes in these parameters with temperature. To derive a rock strength value, we assimilate the normal stress as the confining pressure $P(r)$. In practice, P_w can be taken as 0 since the brittle-ductile transition occurs above the dehydration temperature of rock (see below and Figure 8), such that water does not affect the frictional behavior of rock.

The ductile behavior of crystalline rock at temperature T and pressure P is described by a flow (creep) law of the form [e.g., Weertman *et al.*, 1978; Kohlstedt *et al.*, 1995]:

$$\dot{\epsilon} = A \sigma^n d^{-p} \exp\left(-\frac{Q + PV}{RT}\right) \quad (7)$$

Here $\dot{\epsilon}$ is the strain rate of the material, σ is the differential stress necessary for creep to occur at this rate, A is a dimensionless material parameter, d is the grain size, p is the grain size exponent, Q and V are the creep activation energy and volume of the material, and R is the ideal gas constant. Although typical Earth mantle rheologies incorporate several creep mechanisms in parallel or series combinations [Kohlstedt *et al.*, 1995], experimental measurements on serpentine in the ductile regime are scarce. At the temperatures, pressures, and differential stresses typical of icy dwarf planet cores ($T = 200$ to 1500 K, $P = 10$ to 4000 MPa, $\sigma < 1$ GPa), the relevant flow regime is diffusion creep, even for millimeter-sized grains. Rutter and Brodie [1988] found equation (7) to describe the diffusion creep of serpentinite for T between 573 and 873 K, P between 180 and 300 MPa, grain sizes between 0.1 and 60 μm , and differential stresses between about 5 and 170 MPa, with $A = 10^{5.62}$, $n = 1$, $p = 3$, $Q = 240$ kJ, and $V = 0$ (with σ in MPa and d in microns). These values yield a flow law close to that of wet diffusion creep of olivine compiled by Korenaga and Karato [2008], which included data collected at temperatures from 1473 K to 1573 K, confining pressures from 100 MPa to 2100 MPa, differential stresses from 4 to 410 MPa, strain rates from 10^{-3} to $0.7 \times 10^{-6} \text{ s}^{-1}$, and grain sizes from 1 to 70 μm . Above the dehydration temperature of serpentine, 730 to 900 K [Perrillat *et al.*, 2005; Evans *et al.*, 2013], the relevant flow law becomes that of diffusion creep in olivine in dry conditions. Such a law was also compiled by Korenaga and Karato [2008] and the flow parameters are very similar to those of wet diffusion and those of Rutter and Brodie [1988]. We therefore adopt the flow parameters of Rutter and Brodie [1988], short of measurements at lower T and lower strain rates more representative of conditions inside dwarf planets. The ductile strength is the differential stress σ that causes creep. The ductile strength is typically insensitive to P and $\dot{\epsilon}$ [Kohlstedt *et al.*, 1995], but very sensitive to T , contrary to the brittle strength which is sensitive to P , but not to T .

The rock strength is the lower of its brittle and ductile strengths. It is highest at the brittle-ductile transition (Figure 1). In practice, we find the strain rate $\dot{\epsilon}$ for which the brittle and ductile strengths are equal, and assume cracks are healed past a time $1/\dot{\epsilon}$. At each time step, in cracked grid zones, this $1/\dot{\epsilon}$ timescale is compared to the time elapsed since cracking last occurred; the zone is assumed no longer cracked if the time elapsed is greater than $1/\dot{\epsilon}$. Because $\dot{\epsilon}$ in a given grid zone changes at each time step (primarily due to temperature changes), the code heals cracks by a fractional factor (time elapsed since cracking) $\times \dot{\epsilon}(t)$ at each time step and cracks are removed once the cumulative fraction is 1. Except for this estimation of crack lifetime, the healing fraction has no effect on the geophysics and geochemistry included in the code (e.g., no impact on crack size).

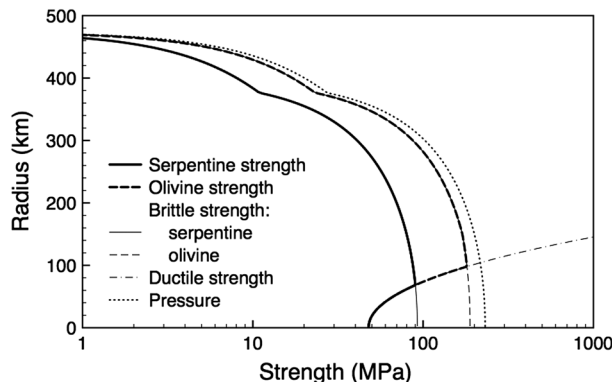


Figure 1. Dry (olivine) and hydrated (serpentine) rock strengths inside a Ceres-type dwarf planet. The olivine brittle strength follows Byerlee's law. The serpentine brittle strength is $\tau = 0.4 P$ [Escartin et al., 1997b]. The ductile strength $\tau = \dot{\epsilon} A d^P \exp[Q/(R T)]$ is derived from Rutter and Brodie [1988]; a strain rate of $(10 \text{ Myr})^{-1}$ and a grain size of $1 \mu\text{m}$ are assumed. The kink in the curves at radius 375 km marks the rocky core–icy mantle boundary in this model.

This equation includes stress relaxation by creep (first right-hand term) and elastic processes (second term). The threshold temperature at which stress starts accumulating is T' , defined such that $\bar{\sigma}(T') = 0$. An approximate analytical expression for T' is

$$T' \approx \frac{Q_{gb}}{R} \left[\ln \left(\frac{96\Omega D_0 \delta_b E}{3^{1/2} n k_b d^3 \bar{T}} \right) \right]^{-1} \quad (9)$$

In equations (8) and (9), Ω is the atomic volume, D_0 and δ_b are the grain boundary diffusion coefficient and width, E is Young's modulus for all grains, k_b is Boltzmann's constant, Q_{gb} is the activation enthalpy, β is the boundary angle, $\Delta\alpha$ is the thermal expansion anisotropy, ν is Poisson's ratio, and n is a fitting parameter.

Let us consider an inclusion within a matrix. If the thermal expansion coefficient of the inclusion is higher than that of the matrix, compressive or tensile stresses will develop upon heating or cooling, respectively.

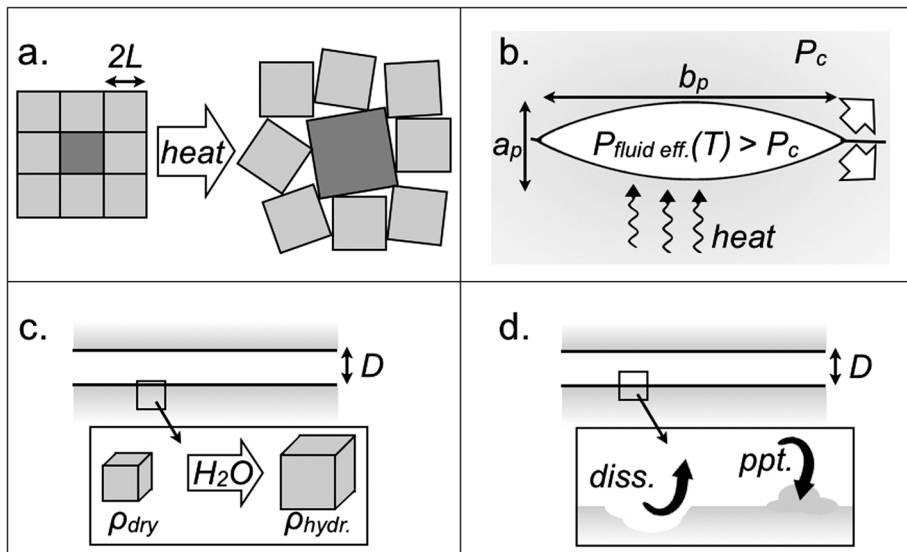


Figure 2. Schematic view of the phenomena included in this study that influence the extent of cracking.
 (a) Microcracking by thermal expansion mismatch of mineral grains.
 (b) Microcracking by expansion of pore water upon heating.
 (c) Microcrack and macrocrack shrinking by hydration swelling of silicates (or widening by dehydration).
 (d) Dissolution and precipitation of mineral species can widen, shrink, or even clog microconduits and macroconduits.

3.2. Microcracking by Thermal Expansion Mismatch

Core microcracks can develop when a rocky core either heats up and expands, or cools and contracts. Vance et al. [2007] modeled the cooling and contraction aspects, but their model holds for heating and expansion as well. We summarize their model, adapted from Evans and Clarke [1980] and Fredrich and Wong [1986].

Thermal expansion anisotropies between square silicate grains result in a mean stress $\bar{\sigma}$ that depends on the cooling rate \dot{T} (Figure 2a). $\bar{\sigma}$ is given by

$$\frac{d\bar{\sigma}}{dT} = \frac{96\Omega D_0 \delta_b E}{3^{1/2} k_b d^3 \dot{T}} e^{-\frac{Q_{gb}}{RT}} \bar{\sigma} - \frac{\beta E \Delta\alpha}{1 + \nu} \quad (8)$$

Table 1. Description of Model Parameters Specific to Dry or Hydrated Silicates

Parameter	Description	Value	Units	References and Notes
<i>Dry Silicates</i>				
E	Young's modulus	200	GPa	Christensen [1966] and Hirth and Kohlstedt [1995]
ν	Poisson's ratio	0.25		Christensen [1966, 1996]
μ_f	Friction coefficient	0.85		Byerlee [1978]; $P < 200$ MPa
		0.6		$P > 200$ MPa
C_f	Cohesive strength	0	MPa	Byerlee [1978]; $P < 200$ MPa
		50	MPa	$P > 200$ MPa
K_{IC}	Fracture toughness	1.5	MPa m ^{1/2}	DeMartin et al. [2004] and Balme et al. [2004]
ρ	Density	3800	kg m ⁻³	Chung [1971]
<i>Hydrated Silicates</i>				
E	Young's modulus	35	GPa	Christensen [1966] and Hirth and Kohlstedt [1995]
ν	Poisson's ratio	0.35		Christensen [1966, 1996]
μ_f	Friction coefficient	0.4		Escartin et al. [1997b]
K_{IC}	Fracture toughness	0.4	MPa m ^{1/2}	Tromans and Meech [2002], Funatsu et al. [2004], Backers [2005], and Wang et al. [2007]
ρ	Density	2600	kg m ⁻³	Tyburczy et al. [1991], Auzende et al. [2006], and Nestola et al. [2010]

This can also occur between two adjacent grains similar in mineralogy, but differing in orientation, that do not undergo isotropic thermal expansion: Bouhifd et al. [1996] showed that thermal expansion coefficient anisotropies could be on the order of $\sim 10^{-6}$ K⁻¹. Microfractures occur when the stress intensity K_I exceeds a critical value, the fracture toughness K_{IC} . K_I is estimated from T and P :

$$K_I = \sqrt{\frac{2}{\pi a}} \int_0^a \frac{\sigma_{yy}(x, T, T') x^{1/2}}{(a-x)^{1/2}} dx - P_c \cdot (\pi a)^{1/2} \quad (10)$$

where a flaw of size $a < d$ extends from the grain boundary ($x = 0$) to $x = a$. P_c is the confining pressure, which tends to reduce stress, and $\sigma_{yy}(x, T, T')$ is the normal stress along the x axis:

$$\sigma_{yy}(x, T, T') = \frac{E\Delta\alpha(T' - T)}{2\pi(1 - \nu^2)} \left(\frac{d^2}{d^2 + (d-x)^2} - \frac{d^2}{d^2 + x^2} + \ln \left[\frac{d-x}{x} \right] - \frac{1}{2} \ln \left[\frac{d^2 + (d-x)^2}{d^2 + x^2} \right] \right) \quad (11)$$

K_I and K_{IC} are substituted to differential stress σ and rock strength τ because crack propagation depends on the product of the differential stress and the square root of flaw length [Griffith, 1921].

The flaw size $a < d$ is chosen so as to maximize K_I . To avoid the calculation of the integral in equation (10) at each grid zone and time step, we tabulate values of $a(K_{I\max})$ separately from the main code for a range of P and T .

Parameter values can be found in Tables 1 and 2. Vance et al. [2007] used parameters for olivine, although one expects cracking to occur also in hydrated serpentine. With increasing hydration, Young's modulus decreases from 200 to 35 GPa and Poisson's ratio increases from 0.25 to 0.35 at room temperature [Christensen, 1966]. The values for both parameters increase only by about 10% or less from 50 to 1000 MPa [Christensen, 1966], and $\partial E / \partial T$ and $\partial \nu / \partial T$ for olivine seem small at room temperature [Kumazawa and Anderson, 1969]. Therefore, we neglect the changes in E and ν with P and T , but not their change with hydration. We adopt values of E and ν linearly interpolated between olivine and serpentine end members (Table 1), depending on the degree of hydration of the silicates. While these values are appropriate for bulk silicates, loosely consolidated rock can have a much smaller Young's modulus.

The fracture toughness of olivine in hydrothermal areas was experimentally determined to be $K_{IC} \approx 0.6 \pm 0.3$ MPa m^{1/2} [DeMartin et al., 2004], which is the value used by Vance et al. [2007]. However, K_{IC} for olivine may be as high as 2 MPa m^{1/2} [Balme et al., 2004; Backers, 2005]. The fracture toughness of clays and salts ranges from 0.1 to 1.5 MPa m^{1/2} [Tromans and Meech, 2002; Backers, 2005; Wang et al., 2007].

Table 2. Description of Model Parameters Not Specific to Dry or Hydrated Silicates

Parameter	Description	Value	Units	References
<i>General Parameters</i>				
D_i	Initial subgrid crack width	10^{-2}	m	
D	Crack width		m	
τ	Rock strength		Pa	
P_c	Confining pressure		Pa	
<i>Brittle-Ductile Transition</i>				
n	Flow law index	1		Rutter and Brodie [1988]
p	Grain size exponent	3		Rutter and Brodie [1988]
d	Grain size	500	μm	Vance et al. [2007]
Q	Flow law activation energy	240 ± 40	kJ	Rutter and Brodie [1988]
A	Flow law coefficient	$10^{5.62}$		Rutter and Brodie [1988]
V	Flow law activation volume	0	m ³	Rutter and Brodie [1988]
$\dot{\epsilon}$	Flow law strain rate		s ⁻¹	Rutter and Brodie [1988]
<i>Thermal Expansion and Contraction Mismatch</i>				
a	Flaw size	$a < d$	m	Vance et al. [2007]
$D_0\delta_b$	Grain boundary diffusion coefficient × Width	$1.5 \times 10^{-0.8}$	m ² s ⁻²	Hirth and Kohlstedt [1995]
K_I	Stress intensity		MPa m ^{1/2}	
n	Fitting parameter	23		Vance et al. [2007]
Q_{gb}	Activation energy for grain boundary creep	3.15×10^5	J mol ⁻¹	Hirth and Kohlstedt [1995]
$\Delta\alpha$	Thermal expansion anisotropy	3.1×10^{-6}	K ⁻¹	Bouhifd et al. [1996]
β	Boundary angle	$\pi/6$	radians	Vance et al. [2007]
Ω	Atomic volume	1.23×10^{-29}	m ³	Hirth and Kohlstedt [1995]
T'	Temperature at zero stress		K	
<i>Thermal Pressurization of Pores</i>				
b_p/a_p	Pore aspect ratio	10 to 10^4		Norton [1984] and Le Ravalec and Guéguen [1994]
α_w	Thermal expansivity of water		K ⁻¹	
β_w	Compressibility of water		Pa ⁻¹	
$P_{\text{fluid eff}}$	Effective fluid pressure		Pa	
<i>Hydration</i>				
$T_{\text{dehydr. min}}$	Temperature at onset of dehydration	700	K	
$T_{\text{dehydr. max}}$	Temperature at onset of hydration	850	K	
$D_{\text{H}_2\text{O}}(T)$	Diffusion rate of water in rock	$4.5 \times 10^{-5} e^{-45000/(RT)}$	m ² s ⁻¹	MacDonald and Fye [1985]
<i>Dissolution and Precipitation</i>				
Ea_{silica}	Activation energy for silica dissolution	62.9 ± 2	kJ	Rimstidt and Barnes [1980]
Ea_{chrys}	Activation energy for chrysotile diss.	70 ± 10	kJ	Thomassin et al. [1977]
Ea_{magn}	Activation energy for magnesite diss.	32.1 ± 3	kJ	Pokrovsky et al. [2009]
V_{silica}	Molar volume of silica	29.0×10^{-6}	m ³ mol ⁻¹	Helgeson et al. [1978]
V_{chrys}	Molar volume of chrysotile	108.5×10^{-6}	m ³ mol ⁻¹	Helgeson et al. [1978]
V_{magn}	Molar volume of magnesite	28.018×10^{-6}	m ³ mol ⁻¹	Helgeson et al. [1978]
μ_i	Rate law parameter	1 or 4 (magnesite)		Pokrovsky and Schott [1999] and Xu and Pruess [2001]
A/V	Area-to-volume ratio	$2/D$	m ⁻¹	Rimstidt and Barnes [1980]
ρ_w	Density of water	1000	kg m ⁻³	
R_j	Rate of reaction		mol m ⁻³ s ⁻¹	
k_i	Rate constant		mol m ⁻² s ⁻¹	
a_j	Activity		Dimensionless or mol m ⁻³ if ideality	
Q_j	Activity product			
K_j	Equilibrium constant			Helgeson et al. [1978]

Funatsu et al. [2004] found that the fracture toughness of sandstone is relatively insensitive to temperature but increases linearly with pressure, from 0.5 to 2.5 MPa m^{1/2} between atmospheric pressure and 10 MPa, which is half of the pressure expected at Ceres' seafloor (Figure 1). In view of these results, we set a canonical value of K_{IC} of 0.4 MPa m^{1/2} for hydrated silicates and 1.5 MPa m^{1/2} for dry silicates. Again, we interpolate linearly between these two end-members, depending on the degree of hydration.

Fredrich and Wong [1986] used values of E , $\Delta\alpha$, v , d , and K_{IC} close to those chosen by *Vance et al.* [2007] and those used here. They showed that the above equations provide a temperature mismatch for the onset of cracking compatible with thermal cracking experiments performed from room temperature up to 1000°C, with typical total increases of order 100°C. Similar temperature changes are predicted by thermal evolution models of Ceres [*Castillo-Rogez and McCord*, 2010], albeit at a much slower rate than in the experiments of *Fredrich and Wong* [1986]. Slow heating allows the rock matrix to relax; this is captured by the use of the temperature of zero stress T' [*Evans and Clarke*, 1980] instead of an initial temperature T_0 in the equations of *Fredrich and Wong* [1986].

3.3. Expansion of Pore Water Upon Heating

In hydrated areas, pore fluid is at confining pressure P_c . However, fluid can expand upon heating. Expansion increases fluid pressure, creating a differential stress that can open microcracks if this stress is higher than the rock strength [*Paterson and Wong*, 2005; *Travis et al.*, 2012] (Figure 2b). We account for pore fluid expansion following *Norton* [1984] and *Le Ravalec and Guéguen* [1994] (see also *Dutrow and Norton* [1995] and *Norton and Dutrow* [2001]). For a temperature increase dT , the fluid pressure P_{fluid} increases by $\partial P/\partial T \times dT$. $\partial P/\partial T$ can be expressed as the ratio of the thermal expansivity of liquid water α_w to its isothermal compressibility β_w [*Norton*, 1984; *Bizzarri and Cocco*, 2006]. Furthermore, because of the elongated shape of pores, the effective stress capable of opening cracks is leveraged at the pore tip by a geometric factor $1 + 2 b_p/a_p$, where b_p/a_p represents the pore aspect ratio, or ratio of the long axis over short axis [*Norton*, 1984]. Thus, assuming the fluid is pure water, the effective fluid pressure at the pore tip is

$$P_{\text{fluid eff}} = P_c + \frac{\alpha_w(T, P_c)}{\beta_w(T, P_c)} dT \times (1 + 2 b_p/a_p) \quad (12)$$

where the subscript w denotes properties for pure water.

For elliptical pores of high aspect ratios, in the limit where microporosity is low and the confining pressure is negligible compared to the rock's Young modulus ($P_c \ll E$), relaxation of the rock matrix mitigates the fluid pressure increase with temperature such that [*Le Ravalec and Guéguen*, 1994, equation (12)]

$$\frac{\partial P}{\partial T} = \alpha_w(T, P_c) \times \left(\beta_w(T, P_c) + \frac{b_p}{a_p} \frac{3(1 - 2v)}{E} \right)^{-1} \quad (13)$$

where $E/[3(1 - 2v)]$ is the rock bulk modulus. Because $\beta_w E \approx 40$ (unless rock is loosely consolidated, in which case E is smaller), the relaxation term is not negligible for aspect ratios b_p/a_p above this threshold. As before, the effective fluid pressure is $P_{\text{fluid eff}} = (\partial P/\partial T) dT \times (1 + 2 b_p/a_p)$.

Cracks open when the differential stress $P_{\text{fluid eff}} - P_c$ exceeds the rock strength τ . This condition is valid in the frame of linear elastic fracture mechanics provided that pore flaw lengths are of order $(K_{IC}/\tau)^2 \sim 1$ mm, such that the differential stress can be assimilated to a stress intensity K_I .

$\alpha_w(T, P_c)$ and $\beta_w(T, P_c)$ are computed from the IAPWS95 equation of state for water [*Wagner and Pruss*, 2002] using the software package CHNOSZ [*Dick et al.*, 2008]. In the model, we set the pore aspect ratio b_p/a_p from 10 [*Le Ravalec and Guéguen*, 1994] to 10⁴ [*Norton*, 1984]. The magnitude of the aspect ratio dictates that of the differential stress $P_{\text{fluid eff}} - P_c$, even though it also favors the elastic relaxation of pores in equation (13).

3.4. Hydration Swelling and Dehydration Shrinking

Incorporation of water molecules into a dry silicate matrix results in swelling of the rock [*Evans et al.*, 2013]. Dehydration leads to shrinking. These phenomena are not often taken into account in models of Earth's hydrothermal systems; perhaps due to the local spatial extent of such models, for which rock is always hydrated. In icy bodies, where hydrothermal systems may extend through the entire core [*Vance et al.*, 2007; *Castillo-Rogez and Lunine*, 2010], the swelling effects of hydration cannot be neglected. We provide a simple set of equations to describe hydration swelling.

Because our 1-D model cannot account for this phenomenon, we incorporate it using a subgrid model: where rock is cracked, we attribute an initial microcrack or macrocrack width D_i , left as a free parameter, to a 2-D crack of infinite length. We assume that hydration occurs in cracked areas to a degree that depends on temperature: full hydration below 700 K, no hydration above 850 K, and a linear decrease between 700 and 850 K. If the degree of hydration has increased since the previous time step, we consider the change in volume of a cube of rock of edge length a undergoing hydration, $a_{\text{hydr}}^3 - a_{\text{dry}}^3$, where the subscripts "hydr" and "dry" refer respectively to more hydrated and drier rock (Figure 2c). This change in volume can be related to a change in crack width D : $\Delta D = -2 \Delta a$, with $\Delta a = [(a_{\text{hydr}} - a_{\text{dry}})/a_{\text{dry}}] a_{\text{dry}}$. The first term can be expressed in terms of the ratio of volumes or densities: $a_{\text{hydr}}/a_{\text{dry}} - 1 = (\rho_{\text{hydr}}/\rho_{\text{dry}})^{-1/3} - 1$. The second term, the cube edge length a , is also the mean distance \bar{x} traveled by a hydration front into the rock after a time step Δt . Thus,

$$\Delta D = -2 \left[\left(\frac{\rho_{\text{hydr}}}{\rho_{\text{dry}}} \right)^{-1/3} - 1 \right] \times \bar{x} \quad (14)$$

The values for ρ_{hydr} and ρ_{dry} depend on the degree of hydration of the silicates. They are linearly interpolated between the values of 2600 kg m⁻³ for hydrated silicates [Tyburczy *et al.*, 1991; Auzende *et al.*, 2006; Nestola *et al.*, 2010] and 3800 kg m⁻³ for dry silicates [Chung, 1971].

We compute $\bar{x}(T)$ following the estimates of MacDonald and Fyfe [1985] from measurements of diffusivities of water molecules in serpentinized peridotites. They found a diffusivity $D_{\text{H}_2\text{O}}(T)$ of $10^{-12} \text{ m}^2 \text{ s}^{-1}$ at 300 K, varying with temperature as $D_{\text{H}_2\text{O}}(T) \approx 4.5 \times 10^{-5} \exp[-(45 \text{ kJ})/(RT)]$. They then estimated the mean distance of diffusive penetration of a hydration front into rock as $\bar{x}(T) \approx (2 D_{\text{H}_2\text{O}}(T) \Delta t)^{1/2}$. After a time step $\Delta t = 50$ years, their approach yields values of \bar{x} of 4 cm at 300 K, up to 4 m at 600 K. Diffusion slows down as $t^{-1/2}$ over longer timescales, relevant for global hydration (see section 5.3.4).

If hydration swelling causes a crack to close, residual swelling generates compression stresses that can open new cracks. The compression stress σ is given by Hooke's law, $\sigma = E\epsilon$, where E is Young's modulus of the rock (Table 1) and $\epsilon = (\Delta D - D)/\bar{x}$ is the compression strain. Cracks open if the differential stress (compression stress minus confining pressure) exceeds the rock strength:

$$E \times \frac{\Delta D - D}{\bar{x}} - P_c(r) > \tau(r) \quad (15)$$

This is a simplification of the analytical compression cracking model of Sammis and Ashby [1986], which successfully reproduced experimental results on the nucleation and growth of cracks on circular pores. Equation (15) holds for grain-sized (mm) cracks (in order to scale rock strength and stress intensity) growing on pores of negligible size.

Dehydration is also accompanied by volume changes in the rock, leading to stresses given by

$$\sigma_{\text{dehydr}} = E \times \left[\left(\frac{\rho_{\text{hydr}}}{\rho_{\text{dry}}} \right)^{-1/3} - 1 \right] \quad (16)$$

If the stress in a given layer exceeds the sum of the confining pressure and rock strength, cracks open. Open cracks may be widened due to dehydration, following equation (14).

3.5. Dissolution and Precipitation of Mineral Species

Once cracks are open, circulation of a chemically reactive aqueous fluid can result in mineral dissolution or precipitation. Dissolution erodes conduit walls and widens microcracks and macrocracks, whereas precipitation narrows or even clogs them. These chemical processes are function of fluid and rock composition, temperature, and pressure. We consider a small number of species: amorphous silica (e.g., from a previous episode of precipitation), the serpentine chrysotile, and the carbonate magnesite. This choice is dictated by two considerations. First, hydrated minerals (perhaps brucite) and carbonates have been observed on the surface of Ceres [Milliken and Rivkin, 2009]. Second, the dissolution reactions involving these species cover a wide range of equilibria (as estimated using thermodynamic data from Helgeson *et al.* [1978]) and kinetic rates [Rimstidt and Barnes, 1980; Thomasson *et al.*, 1977; Pokrovsky *et al.*, 2009], and therefore can be used as proxies to explore the impact of other reactions on crack width. No attempt was

made at accurately modeling the chemistry of water-rock reactions, such as chemical feedbacks between reactions or the effect of pH. We consider the following reactions:



These reactions are reversible (precipitation). Each has an equilibrium constant $K_i(T, P)$, determined at local temperature and pressure using the software package CHNOSZ (*Dick et al. [2008]*; thermodynamic data from *Helgeson et al. [1978]*). Above the transition temperature of amorphous silica (622 K), we consider the dissolution of quartz, which is the stable SiO_2 species between 622 K and 867 K for $P < 5$ kbar. (Above 850 K, the rock is assumed dehydrated and dissolution is irrelevant.) α quartz and β quartz are considered in their stability regimes [*Helgeson et al., 1978*].

At low temperatures possible in dwarf planet oceans (200 K $< T < 273$ K), we assume water remains liquid due to the presence of antifreezes. Thermodynamic data below 273 K are scarce, and the equation of state for pure water, needed for CHNOSZ computations, has to be extrapolated [*Wagner and Pruss, 2002*; *Neveu et al., 2015*]. Therefore, where local temperatures are below 261 K, we set $T = 261$ K for the determination of $K_i(T, P)$. We neglect the heats of dissolution and precipitation in the local heat budget.

At such low temperatures, chemical reactions may be controlled by kinetics rather than thermodynamic equilibria. Modeling suggests that kinetics can dominate equilibrium even for Earth's hydrothermal systems [*Bolton et al., 1999*]. The kinetics of silica dissolution have been studied by *Rimstidt and Barnes [1980]*, who found the precipitation rate $R_{\text{SiO}_2 \text{ ppt}}$ to be proportional to the activity of dissolved aqueous silica $a_{\text{SiO}_2 \text{ (aq)}}$ and to the ratio A/V of fluid-rock contact surface area to fluid volume (assuming a constant fluid density $\rho_w = 1000 \text{ kg m}^{-3}$). Thus,

$$R_{\text{SiO}_2 \text{ ppt}} = k_{\text{SiO}_2 \text{ ppt}}(T) (A/V) a_{\text{SiO}_2 \text{ (aq)}} \quad (17)$$

The proportional term, $k_{\text{SiO}_2 \text{ ppt}}(T)$, is a rate "constant" (units of $\text{mol m}^{-2} \text{ s}^{-1}$) which follows an Arrhenius law $\exp[-E_a/(RT)]$, where E_a is an activation energy and R is the ideal gas constant.

Likewise, the dissolution rate is proportional to the activity of solid silica, which is 1 for the pure crystalline solid. We assume an activity of 1 for amorphous silica as well. The net dissolution rate $R_{\text{SiO}_2} = (\partial a_{\text{SiO}_2 \text{ (aq)}} / \partial t)_{P, T, V}$ (dissolution minus precipitation) is therefore

$$R_{\text{SiO}_2} = (A/V) [k_{\text{SiO}_2 \text{ diss}} a_{\text{SiO}_2(s)} - k_{\text{SiO}_2 \text{ ppt}} a_{\text{SiO}_2 \text{ (aq)}}] \quad (18)$$

where the subscript "diss" denotes dissolution. This expression can be simplified using the activity product $Q_i = \prod a_i^{\nu_i}$, where ν_i are the stoichiometric coefficients. With $a_{\text{SiO}_2(s)} = 1$, we have $Q_{\text{SiO}_2} = a_{\text{SiO}_2 \text{ (aq)}}$. Therefore,

$$R_{\text{SiO}_2} = (A/V) k_{\text{SiO}_2 \text{ diss}} \left[1 - \frac{Q_{\text{SiO}_2}}{K_{\text{SiO}_2}(T, P)} \right] \quad (19)$$

At equilibrium, $Q_{\text{SiO}_2} = K_{\text{SiO}_2}$ and the net rate is zero. The dissolution and precipitation rate constants are linked via the equilibrium constant: $k_{\text{SiO}_2 \text{ ppt}}(T) = k_{\text{SiO}_2 \text{ diss}}(T) / K_{\text{SiO}_2}(T, P)$, so the precipitation rate constant depends on pressure. For any reaction where the reactants have an activity of 1, equation (19) becomes:

$$R_i = (A/V) k_i \text{ diss} \left[1 - \left(\frac{Q_i}{K_i(T, P)} \right)^{\mu_i} \right] \quad (20)$$

We have followed the derivation of *Rimstidt and Barnes [1980]*. *Xu and Pruess [2001]* provided a more general version of equation (20) that takes into account, for example, the effect of mineral reactive surface area at

different water saturations. Sometimes, the dependence of R_i on Q_i/K_i is nonlinear and experimental data are fitted by a law with $\mu_i \neq 1$ [Xu and Pruess, 2001].

The activation energies of the dissolution rate constants at atmospheric pressure have been determined experimentally: 62.9 kJ for amorphous silica [Rimstidt and Barnes, 1980], about 70 kJ for chrysotile [Thomassin et al., 1977; Bales and Morgan, 1985, Figure 4], and about 32 kJ for magnesite [Pokrovsky et al., 2009, Table 4]. The magnesite value is valid at a pH of 5.4 and decreases with both pH and (to a lesser extent) $p\text{CO}_2$; based on the Figure 2 of Pokrovsky and Schott [1999], a more general expression for the rate constant of magnesite dissolution may be $k_{\text{MgCO}_3 \text{ diss}} = 10^{-0.3(\text{pH}-5.4)} \times \exp[-E_a/(RT)]$. Because these reactions do not involve gases, their rates do not depend much on pressure. For silica and chrysotile $\mu_i = 1$, but for magnesite $\mu_i = 4$ [Pokrovsky and Schott, 1999].

To account for the impact of chemical reactions on crack width, we adopted the same subgrid approach as for the hydration process. Thus, the crack width D changes as a result of both hydration and dissolution (Figure 2d). For our 2-D crack geometry, the area to volume ratio A/V is $2/D$ [Rimstidt and Barnes, 1980]. The net change in crack width after a time Δt due to chemical processes is [Rimstidt and Barnes, 1980, equation (61); Martin and Lowell, 2000]

$$\Delta D = \sum_{i=1}^{N_{\text{species}}} \frac{R_i \Delta t V_i(T, P)}{[A/V]} \quad (21)$$

where V_i is the molar volume of the mineral species dissolved, which we take at 298 K and 1 bar from Helgeson et al. [1978]. We assume negligible salinity, so that activities are assimilated as molalities (moles per kilogram of water) and R_i has units of $\text{mol m}^{-3} \text{ s}^{-1}$. The change in species activity (molality) after a time Δt is $\Delta a_i = v_i R_i \Delta t / \rho_w$. If a species precipitates entirely, $\Delta a_i = -a_i$ and the variation in D from the precipitation of this species is

$$\Delta D_i = \frac{\Delta a_i \rho_w V_i(T, P)}{v_i [A/V]} \quad (22)$$

In the code, we allow chemical reactions only in zones of hydrothermal circulation. Changes in D_i , R_i , and a_i feed back on each other on timescales possibly shorter than the geophysical code time step (typically 50 years). To capture these feedbacks, we iterate calculations of crack widths, dissolution rates, and activities using equations (20) through (22) over a short chemical time step, typically 10^{-6} times the main geophysical time step. After a few iterations, ΔD_i and Δa_i may converge toward values that are then scaled to the geophysical time step. Alternatively, precipitation may occur, either because T and P have changed since a previous time step at which species were in solution or because the reaction timescale is much shorter than even the chemical time step. In the former case, the crack is closed. In the latter case, dissolution and precipitation cancel each other: the net sum of D_i in equations (21) and (22) is zero. In this case, chemical processes are decoupled from cracking processes and have no influence on geophysics.

3.6. Neglected Effects

3.6.1. Thermal Expansion of the Rock Matrix

Rock can expand upon heating; this affects cracking. Thermal expansion coefficients of silicates are of order 10^{-5} K^{-1} , about 2 orders of magnitude smaller than that of water [Germanovich et al., 2001]. A temperature increase of 100 K will thus cause a relative rock volume increase of 0.1%. This is small compared to the rock volume increase resulting from hydration, $\rho_{\text{hydr}}/\rho_{\text{rock}} - 1 \approx 30\%$. Thermal pressurization of pores is also likely to dominate rock expansion even at low water-to-rock ratios.

3.6.2. Fluid Pressure Changes Linked to Conduit Size

Any pressure change due to a change in crack size should bear mostly on the fluid, because the compressibility of even highly porous serpentine is 2 orders of magnitude lower than that of water [Hilairet et al., 2006; Walsh, 1965; Kelemen and Hirth, 2012]. We assume that fluid percolates away before precipitation causes the rock to become cemented, such that “geyser”-like conduits never occur.

3.6.3. Anisotropy in Rock Permeability

We do not consistently model the geometry, orientation, and connectivity of cracks, and do not account for anisotropies in rock permeability. At the submillimeter scale, the degree of anisotropy in crack orientation seems low [Boudier et al., 2010; Hanowski and Brearley, 2001]. Bolton et al. [1997, 1999] considered the impact of a nonhomogeneous and anisotropic permeability on hydrothermal flow and found that fluids flow so as to connect regions of higher permeability.

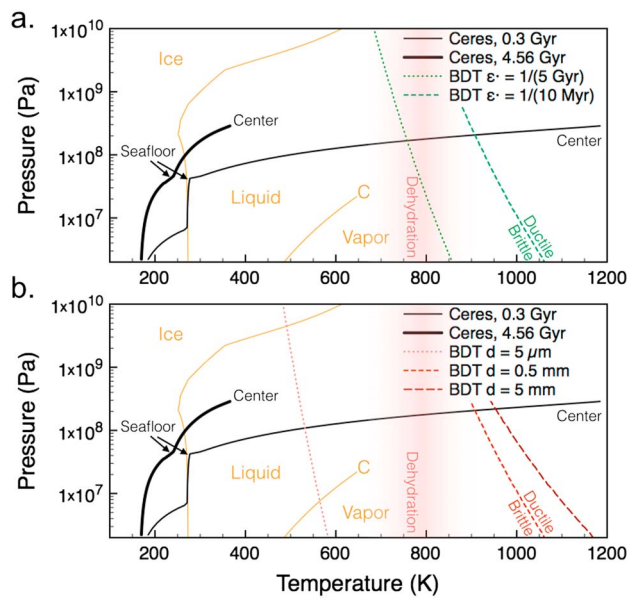


Figure 3. (a) Dashed and dotted curves: Brittle-ductile transition (BDT) in silicates for various strain rates, assuming a grain size of $500 \mu\text{m}$ [Rutter and Brodie, 1988]. (b) Dashed and dotted curves: BDT for various grain sizes, assuming a strain rate of $(10 \text{ Myr})^{-1}$. Solid black curves: Pressure-temperature (P - T) profiles inside Ceres obtained using the present thermal evolution model, after 0.3 Gyr (hottest profile) and 4.56 Gyr of evolution. Solid orange curves: Phase diagram of pure water. Dehydration and the brittle-ductile transition both occur above (but close to) the critical temperature for pure water for most parameters.

from the Sun than the Earth and could have accreted a higher proportion of volatiles [Desch *et al.*, 2009; Castillo-Rogez and McCord, 2010; Sohl *et al.*, 2010], some of which have a lower vapor pressure than water. Thus, careful treatment of gas processes should include not only water vapor but also primordial volatiles and those formed as a consequence of endogenic activity, such as ammonia, methane, molecular hydrogen, or carbon dioxide [Neveu *et al.*, 2015]. We leave the inclusion of these species for future work.

Although we do not model phase separation, Goldfarb and Delaney [1988] suggested that brines precipitate preferentially on conduit walls and cracks close from the outside in, with the smaller conduits shutting off first; this is an implicit assumption of our model.

3.6.5. Species Transport

Species transported in the hydrothermal flow may not dissolve and precipitate in the same place. One expects more dissolution at depth, and precipitation in shallower layers where solubilities are decreased at lower temperatures and pressures. In our code, typical grid spacing and time step are 2 km and 50 years. The timescale of hydrothermal transport can be estimated using equation (26). Setting $\kappa = 10^{-15} \text{ m}^2$, $\mu = 10^{-3} \text{ Pa s}$, $\Phi = 0.01$, and $\partial P/\partial r = 10^3 \text{ Pa m}^{-1}$, one finds $v = 10^{-7} \text{ m s}^{-1}$ or 160 m in 50 years, an order of magnitude less than the grid spacing. Therefore, the approximation of no transport holds for permeabilities of 10^{-15} m^2 or lower. If 1-D vertical velocities are much higher than 1 km per century, one can assume that concentrations are homogenized in circulating layers. If the ratio of grid spacing to time step is comparable to flow velocity, tracking concentrations with transport equations is necessary [e.g., Travis *et al.*, 2012], as chemical stratification occurs in the long term. A posteriori, our simulations of Ceres do suggest permeabilities consistent with nonnegligible species transport and possible chemical stratification. As previously mentioned, such accurate modeling of hydrothermal chemistry falls outside the scope of this paper and is left for future work.

3.6.6. Anisotropy in Serpentine Properties

The crystalline structures of serpentine minerals are anisotropic; this is reflected in their physical properties [Hilairet *et al.*, 2006]. We assume that in large volumes of rock, these properties are averaged over all possible directions. This assumption holds for macroscopic cracking phenomena, such as compressive stresses

3.6.4. Gas Processes and Multiphase Flows

The presence of vapor can lead to brine segregation in the liquid phase, which favors precipitation. Vaporization of fluid in segregated pores results in large pore pressure increases, leading to fracturing. Liquid-vapor equilibria also influence fluid chemistry and fluid-rock interactions. For these reasons, all state-of-the-art models of hydrothermal systems incorporate gas effects [Goldfarb and Delaney, 1988; Xu and Pruess, 2001; Ingebritsen *et al.*, 2010; Han *et al.*, 2013]. At this time we have ignored gas processes, including volatile exsolution [Kelley *et al.*, 1993], gas diffusion in the rock matrix, gas-solute reactions and resulting fluid pressure changes, two-phase permeabilities, and capillary pressure [Ingebritsen *et al.*, 2010]. This choice is justified in part because hydrothermal systems may be cooler on icy dwarf planets than on Earth, at a given pressure. If the brittle-ductile transition occurs below the critical temperature for pure water, supercritical effects are irrelevant (Figure 3). On the other hand, Ceres formed further away

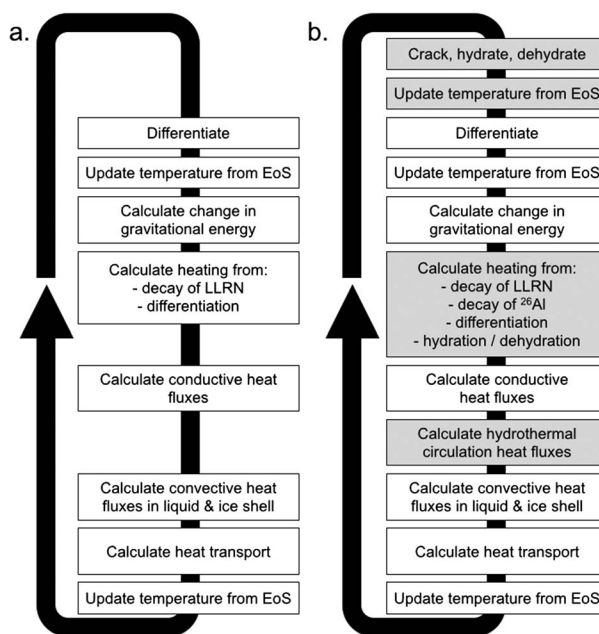


Figure 4. (a) Calculations carried at each time step in the thermal evolution code of Desch *et al.* [2009]. (b) Updates to the code are shown in grey boxes. EoS = equation of state; LLRN = long-lived radionuclides.

resulting from hydration swelling. For microscopic phenomena, such as thermal expansion mismatch at grain boundaries and thermal pore pressurization, stress buildup and brittle deformation occur in a preferred direction. Elasticity and failure properties quoted in Table 1 were determined from experiments on macroscopic samples, and thus account empirically for anisotropy. For example, measured values of K_{IC} are likely those for the weakest axis, along which brittle failure first occurs [Escartin *et al.*, 1997b].

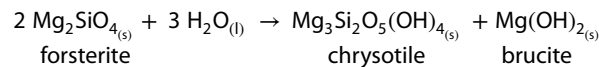
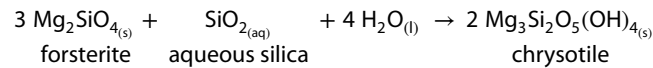
4. Inclusion in Thermal Evolution Code

To study feedbacks between core cracking and thermal evolution, we have modified the code of Desch *et al.* [2009] to include the cracking model described above. The upgrades are shown in Figure 4. The updated code is freely available at <https://github.com/MarcNeveu/IcyDwarf>.

4.1. Rock Hydration and Dehydration

The cracking model accounts for silicate hydration, which was not modeled by Desch *et al.* [2009]. We have modified their 1-D code so that hydrated silicates in a given layer dehydrate if the temperature of that layer exceeds 700 K. To smooth out the transition between dry and hydrated rock, we have defined a degree of hydration X_{hydr} in each layer, which is 0 if the silicates in this layer are completely dehydrated and 1 if the silicates are fully hydrated. For dehydrating silicates, X_{hydr} decreases linearly with temperature between 700 K and 850 K. X_{hydr} is allowed to increase in a given layer only if (a) the temperature of this layer is below 850 K and decreasing, (b) this layer is cracked, as well as all core layers above, so that it is possible for liquid water above the seafloor to flow down core cracks to reach the layer, and (c) there is enough liquid to hydrate this layer.

Upon hydration or dehydration, heat is produced or consumed, respectively. The amount of heat released, H_{hydr} , was estimated using CHNOSZ by calculating enthalpies of reaction $\Delta_r H$ at temperatures between 700 and 850 K and pressures between 100 and 5000 bar (10 and 500 MPa), for the following two hydration reactions:



At these temperatures and pressures, enthalpies of reaction range between -450 and -700 kJ/kg of forsterite consumed, with similar values if the serpentine product is antigorite. The midrange value, -575 kJ/(kg⁻¹ dry silicate), was arbitrarily chosen for H_{hydr} . The net heating rate Q_{hydr} is calculated in each layer with rock mass M_{rock} as

$$Q_{hydr} = \Delta X_{hydr} \times M_{rock} \times (-H_{hydr}) / \Delta t \quad (23)$$

This heat of hydration is added to those arising from radioactive decay and changes in gravitational potential in equation (1).

The degree of hydration of silicates influences their thermal conductivity. Hydrated rocks and chondritic material have conductivities of 0.5 to 1.5 W m⁻¹ K⁻¹ [Yomogida and Matsui, 1983; Clauser and Huenges, 1995; Opeil et al., 2010]; for dry silicates a value of 4.2 W m⁻¹ K⁻¹ has been adopted by many modelers [Ellsworth and Schubert, 1983; McCord and Sotin, 2005; Robuchon and Nimmo, 2011; Guilbert-Lepoutre et al., 2011]. We choose the values of 1 W m⁻¹ K⁻¹ for hydrated rock and 4.2 W m⁻¹ K⁻¹ for dry rock. The thermal conductivity of partially hydrated rock varies linearly with X_{hydr} between these two values.

The hydration and dehydration subroutines move mass and internal energy of water and rock on the 1-D grid but do not update grid temperatures. Thus, after these subroutines are called, temperatures are updated in each grid zone using the relevant equations of state for each material (Figure 4).

4.2. Hydrothermal Circulation in the Cracked Layer

If parts of the core in contact with a liquid ocean are cracked, cooler water can circulate down into the core fractures, warm up, and return to the ocean in a convective pattern known as hydrothermal circulation. This phenomenon results in mass and energy transfer in and out of the core. In our models, hydrothermal circulation occurs in the cracked layers in contact with the ocean if (a) there is enough liquid to be circulated (i.e., the volume of liquid is greater than the volume of pores in the cracked rock); and (b) the Rayleigh number Ra exceeds the critical Rayleigh number for convection in a porous medium with a permeable top, about 30 [Lapwood, 1948; Ribando et al., 1976; Cherkaoui and Wilcock, 2001]. In a porous medium, Ra can be expressed as [Phillips, 1991]

$$Ra = \frac{\alpha_w \rho_w^2 c_p g \Delta T \kappa \Delta r}{k_w \mu} \quad (24)$$

with $c_p = 4188.5 \text{ J kg}^{-1} \text{ K}^{-1}$ the heat capacity of water, g the gravitational acceleration, calculated in the middle of the hydrothermal layer of thickness Δr , ΔT the temperature gradient across the layer, κ the permeability of the medium (in m²), $k_w = 0.61 \text{ W m}^{-1} \text{ K}^{-1}$ the thermal conductivity of liquid water, and μ the dynamic viscosity of the fluid.

We model circulation in a greatly simplified fashion. Mass transfer is neglected under the assumption of negligible species transport and steady state fluid circulation. Convective heat transfer is not modeled explicitly, but parameterized in the form of an increased effective thermal conductivity for the layers experiencing hydrothermal circulation. This effective thermal conductivity, k_{hydro} , is derived from the following equations:

$$\frac{\partial T}{\partial t} = \frac{1}{\rho_w c_p} \frac{\partial}{\partial r} \left(k_{\text{hydro}} \frac{\partial T}{\partial r} \right) \quad (25)$$

$$v = \frac{dr}{dt} = \frac{1}{\Phi \mu} \frac{\kappa}{\partial P} \frac{\partial P}{\partial r} \quad (26)$$

Equation (25) describes conductive heat transport. Equation (26), Darcy's law, describes fluid flow in a porous medium in response to a pressure gradient $\partial P / \partial r$. The 1-D fluid velocity is v , and Φ is the dimensionless bulk medium (rock) porosity. We assume for simplicity that the fluid is moved by the lithostatic pressure gradient. In reality, the pressure of fluid circulating through cracks should follow a hydrostatic gradient several-fold shallower [Kelley and Delaney, 1987]. However, thermal expansion of the fluid increases its pressure at depth, which steepens the fluid pressure gradient up to several folds, depending on core temperatures.

Assuming temperature and pressure variations ΔT and ΔP are small across a layer, these equations can be rearranged to give k_{hydro} :

$$k_{\text{hydro}} = \frac{\rho_w c_p}{\Phi} \frac{\kappa}{\mu} \frac{\Delta P}{\Delta T} \quad (27)$$

With $\Phi = 30\%$, $\kappa = 10^{-12}$ to 10^{-15} m², $\mu = 10^{-3}$ Pa s, $\rho_w = 1000 \text{ kg m}^{-3}$, $c_p = 4188 \text{ J kg}^{-1} \text{ K}^{-1}$, $\Delta P = 10^5$ to 10^6 Pa , one finds $k_{\text{hydro}} = 1$ to $10^4 \text{ W m}^{-1} \text{ K}^{-1}$.

Table 3. Description of Hydrothermal Circulation Parameters

Parameter	Description	Value	Units	References and Notes
Φ	Bulk porosity of fractured silicate layer	0.01		
κ	Permeability of fractured silicate layer	10^{-15}	m^2	Fisher [1998]
k_{hydro}	Maximum effective thermal conductivity of layers experiencing hydrothermal circulation	100	$\text{W m}^{-1} \text{K}^{-1}$	May be lower than actual value to keep code stable
Ra_{cr}	Critical Rayleigh number for convection in a porous medium	30		Lapwood [1948], Ribando <i>et al.</i> [1976], and Cherkaoui and Wilcock [2001]

In practice, we cap k_{hydro} at $100 \text{ W m}^{-1} \text{ K}^{-1}$ to avoid destabilizing the code with large energy transfers by violating the Courant condition. If k_{hydro} is much larger than material thermal conductivities, its exact value matters little: even at $100 \text{ W m}^{-1} \text{ K}^{-1}$, layers undergoing circulation quickly become nearly isothermal, the bottleneck of heat transfer being in nonhydrothermal solid layers. In the calculation of k_{hydro} , we assume $\Phi = 0.01$ and that κ varies as the square of crack size D [Millington and Quirk, 1961]: $\kappa = 10^{-15} \times [D/(1 \text{ mm})]^2 \text{ m}^2$ (Table 3). In zones that are not cracked, the code prevents hydrothermal circulation from taking place; this is equivalent to setting $\Phi = 0$ and $\kappa = 0$. The value of Φ in cracked zones is chosen low enough that circulation is not impeded by lack of liquid, in case liquid contained in a thin layer must circulate through the entirely cracked (porous) core. The value of κ for 1 mm cracks is anchored arbitrarily in the middle of the range of measured seafloor rock permeabilities, which spans over 10 orders of magnitude [Fisher, 1998]. The importance of choosing an appropriate order of magnitude for κ is mitigated in our approach by the need to cap k_{hydro} . This coarse treatment of permeability and hydrothermal heat transfer could be improved, but at the expense of modeling hydrothermalism on a global scale and over geologic time, as meeting the Courant condition at high k_{hydro} would require coarsening the grid or decreasing the time step by orders of magnitude.

The viscosity of the liquid, $\mu(T)$, is key in determining the effective thermal conductivity. At low temperature, water-ammonia liquids have much larger viscosities, 10 to 100 Pa s, than does liquid water at 293 K (1.00×10^{-3} Pa s). We adopt the empirical formulation of Kargel *et al.* [1991] for $\mu(T)$ in Pa s. This fit to their experimental data matches their measurements to 15% or less, for ammonia mass fractions X from 0 to 100% and temperatures from 176 K to 340 K:

$$\mu = \exp(A + B/T) \quad (28)$$

with, for $T > 240$ K:

$$A = -10.8143 + 0.711062X - 22.4943X^2 + 41.8343X^3 - 18.5149X^4 \quad (29)$$

$$B = 1819.86 + 250.822X + 6505.25X^2 - 14,923.4X^3 + 7141.46X^4 \quad (30)$$

and for $T < 240$ K

$$A = -13.8628 - 68.7617X + 230.083X^2 - 249.897X^3 \quad (31)$$

$$B = 2701.73 + 14,973.3X - 46,174.5X^2 + 45,967.6X^3 \quad (32)$$

Other model parameters relevant to hydrothermal circulation are listed in Table 3.

We coarsely model heat transfer by convection in liquid, following Desch *et al.* [2009], by imposing an effective thermal conductivity of $400 \text{ W m}^{-1} \text{ K}^{-1}$ wherever the melt fraction exceeds 2%. This allows us to run the code with a reasonably large time step without violating the Courant condition and results in a temperature gradient across the convecting liquid layer of less than 5 mK km^{-1} for a typical heat flux of 2 mW m^{-2} , which is negligible compared to that across silicate, hydrothermal, or icy layers. Such a negligible temperature drop is consistent with more sophisticated simulations of subsurface ocean convection [Goodman and Lenferink, 2012; Travis *et al.*, 2012]; therefore, even our crude treatment should provide a good approximation of spatially averaged heat transfer across potential liquid layers.

Table 4. Description of Thermal Model Parameters

Parameter	Description	Value	Units	References and Notes
t_0	Accretion time after CAIs	2, 3, or 5	Myr	Castillo-Rogez and McCord [2010]
T_{surf}	Surface temperature	168	K	Effective temperature at 2.7 AU with albedo 0.02
T_{init}	Initial temperature	168	K	Assumed no accretional heat
T_{diff}	Final differentiation temperature	140	K	Rubin et al. [2014]
R	Radius	475	km	$R_{\text{mean}} = 471 \pm 5$ km [Drummond et al., 2014]
ρ	Bulk density	2077	kg m^{-3}	Castillo-Rogez and McCord [2010]
X	$\text{NH}_3/\text{H}_2\text{O}$ mass fraction	$10^{-10}, 0.01$		Desch et al. [2009] and Castillo-Rogez and McCord [2010]
$(X_{\text{hydr}})_0$	Initial degree of hydration	1		Fully hydrated [Castillo-Rogez and McCord, 2010]
k_{dry}	Thermal conductivity, dry rock	4.2	$\text{W m}^{-1} \text{K}^{-1}$	Ellsworth and Schubert [1983]
k_{hydr}	Thermal conduct., hydrated rock	1	$\text{W m}^{-1} \text{K}^{-1}$	Clauser and Huenges [1995]

5. Results

5.1. Thermal and Geophysical Evolution of Ceres

We have modeled the thermal and geophysical evolution of Ceres from immediately after its accretion until present (4.56 Gyr). Canonical parameters were assumed for the cracking model (Tables 1 and 2) and for the thermal model (Tables 3 and 4). We assumed that Ceres accreted “cold” (no heat of accretion), from hydrated planetesimals.

Three scenarios illustrate different outcomes in Ceres’ evolution depending on the amount of internal heating from the decay of the short-lived radionuclide ^{26}Al . Major ^{26}Al heating occurs if Ceres accretes at $t_0 = 2$ Myr after the formation of calcium-aluminum inclusions (CAIs); this is scenario (a). In scenario (b), $t_0 = 3$ Myr and ^{26}Al heating is more moderate. In scenario (c), $t_0 = 5$ Myr and ^{26}Al heating is even lower. These three scenarios were chosen identical to those investigated by Castillo-Rogez and McCord [2010] to facilitate comparisons between model outcomes.

In all three scenarios, differentiation occurs quickly. It is initiated by ice melting in the central regions of Ceres, which occurs between 0.1 Myr (scenario (a)) and 18 Myr (scenario (c)), even in the absence of antifreezes, out to a radius of at least 375 km. This leads to a gravitationally unstable configuration, with an undifferentiated outer shell overlying an icy mantle. Rubin et al. [2014] have shown that in this situation, differentiation then proceeds by Rayleigh-Taylor instabilities (foundering) at temperatures $T_{\text{diff}} = 140 \pm 20$ K. This is lower than Ceres’ starting and surface temperatures, set at 168 K. Therefore, differentiation is instantaneous once the Rayleigh-Taylor configuration is set up. We consider that differentiation proceeds by foundering once Ceres’ interior is differentiated out to a radius $R/2$.

5.1.1. Simulations With Negligible NH_3 Amounts

Here the ice component is assumed to contain negligible amounts of ammonia (mass fraction 10^{-10} with respect to water). Results for the three scenarios are shown in Figure 5.

In scenario (a), ^{26}Al decay delivers enough heat to immediately crack the entire hydrated core by pore water pressurization, no matter the pore aspect ratio. ^{26}Al decay heating also triggers dehydration of the silicate core after about 0.5 Myr (Figure 5a). Dehydration is complete by 2.5 Myr, also fractures the entire core, and consumes much radiogenic heat. However, it releases liquid water as an ocean surrounding the core, and the hydrosphere of Ceres is almost entirely melted. Past 2.5 Myr, only the upper 10 km of the core are cracked (Figure 6a): there, the highest temperatures reached are still low enough ($T < 400$ K) that rock remains brittle on timescales much longer than the age of the solar system (Figure 8). Hydrothermal circulation is prevented in these brittle layers by mineral precipitation, which clogs cracks in the second outermost core layer (Figure 6a). Inner core regions keep heating until about 300 Myr (peak temperature around 1180 K). Subsequently, Ceres quickly cools as a whole. Past 1.2 Gyr, temperatures in the entire core are low enough to allow rehydration. Surprisingly however, despite large amounts of liquid, rehydration does not occur. This is because thermal contraction mismatch does not yield high enough stresses to further crack core silicates. Stress intensities K_I from contraction mismatch range from a few $10^5 \text{ Pa m}^{1/2}$ just below the cracked layer to $10^4 \text{ Pa m}^{1/2}$ further down. This is close to, but lower than, the fracture toughness K_{IC} for dry and hydrated silicates. Thus, core cooling occurs slowly enough that stresses arising from thermal

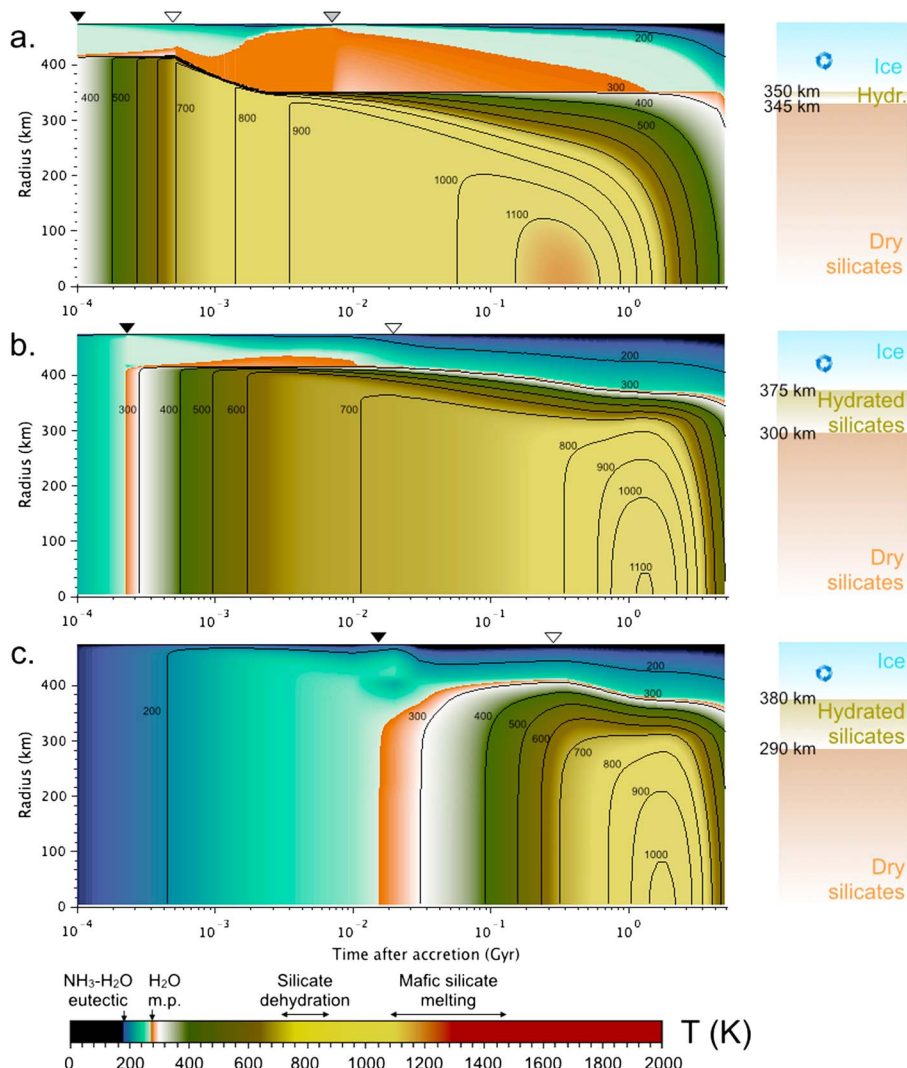


Figure 5. (left) Thermal evolution of Ceres in three cases: accretion (a) 2 Myr, (b) 3 Myr, and (c) 5 Myr after the condensation of Ca-Al inclusions (CAIs). A negligible $\text{NH}_3\text{-H}_2\text{O}$ mass fraction of 10^{-10} is assumed. Black arrows on top of each panel indicate the onset of differentiation. White arrows indicate the onset of dehydration, around 700 K. In Figure 5a, the gray arrow indicates a brief episode of hydrothermal circulation. (right) Present-day structures of Ceres. Circular arrows indicate convective heat transfer in the corresponding layers.

expansivity mismatch between adjacent grains of differing mineralogy are accommodated by diffusion creep before cracking occurs. Since rehydration does not occur, the final core radius is small: 350 km. Outer hydrosphere layers slowly refreeze and subsolidus convection in ice is initiated after 4.25 Gyr, once liquid convection and hydrothermal circulation cease. Together, solid state convection in ice, convection in the ocean, hydrothermal circulation, and the high thermal conductivity of dehydrated silicates all contribute to cooling Ceres to a greater extent than in the other two scenarios, yielding a cold present state (central temperature around 385 K at 4.56 Gyr). Present-day hydrosphere temperatures range between 168 K and 220 K, too low to maintain liquid without antifreezes.

In scenario (b), the entire hydrated core is still cracked by pore pressurization immediately after differentiation at 0.2 Myr. Due to weaker heating by ^{26}Al decay, core dehydration is much slower, starting at 20 Myr and stopping at 1.2 Gyr when peak core temperatures are reached. Dehydrating areas are fractured. Dehydration is incomplete and yields a dry inner core of radius 300 km surrounded by a hydrated outer core 75 km thick. Cracks that opened prior to core dehydration heal quickly in the dehydrated zone, where temperatures are above 850 K (Figure 8), but persist in the hydrated layers (Figure 6b). Liquid convection

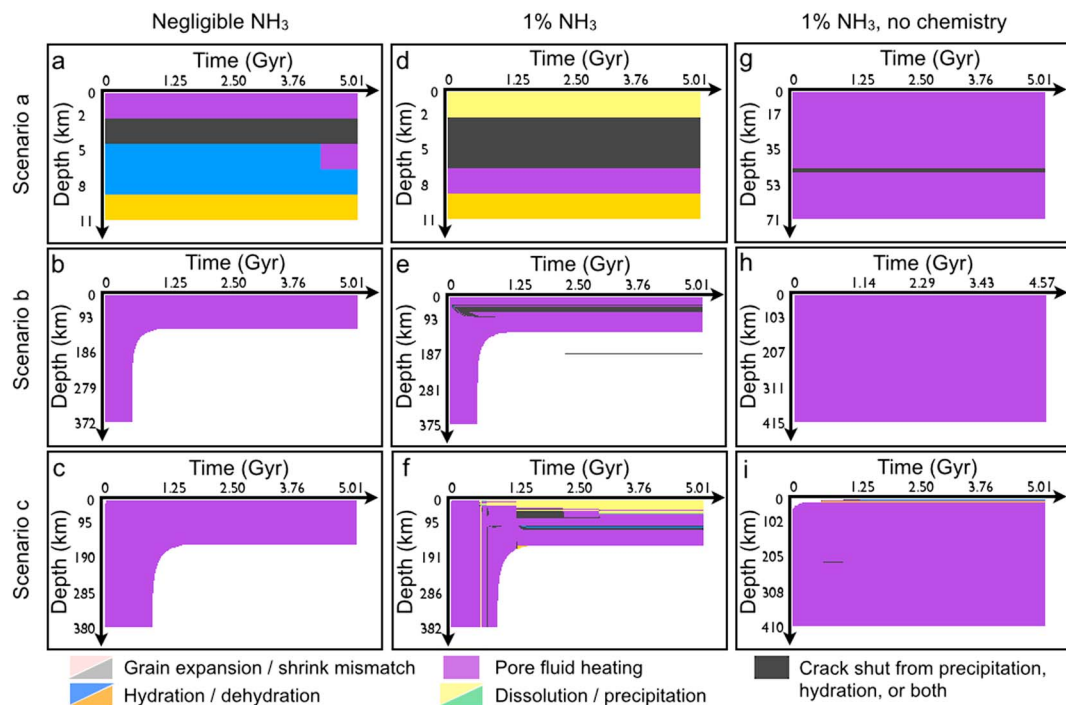


Figure 6. Depth of cracking inside Ceres' core over geologic time. The depth is 0 at the seafloor and increases toward the center. Note the different vertical scales, which depend on maximum cracked depth (core radii are shown on Figures 5 and 7). Cracking by thermal pore pressurization generally dominates. Dehydration cracking is also widespread (see text), but not shown here if it occurs in zones already fractured by pore pressurization. Cracking by hydration swelling seldom occurs, and cracking by thermal mismatch does not occur. (a) Precipitation shuts off cracks in the second outermost zone (grid resolution 2.4 km), preventing circulation in the underlying zones. (b, c, e, and f) Cracks heal due to ductile creep in the hot central zones. (d, e, and f) Crack clogging by precipitation, sometimes aided by hydration swelling, yields impermeable layers in the core (see text for details). (g) A layer is made impermeable solely by hydration swelling, as precipitation was disabled in this simulation. (h and i) The entire core remains fractured until the present day.

is initiated as soon as Ceres differentiates but ceases after only 10 Myr, short of liquid as the hydrosphere refreezes. Ice convection, also initiated immediately after differentiation, persists weakly until present. Hydrothermal circulation never occurs. Present-day core temperatures are higher than in scenario (a), with a central temperature around 550 K. Although this is cold enough for the core to be rehydrated, late hydration does not occur since there is no liquid.

In scenario (c), differentiation and core cracking take more time. The brittle, hydrated core is entirely cracked by pore thermal pressurization after 20 Myr (Figure 6c). Partial dehydration is initiated after 300 Myr (Figure 5c), cracking the dehydrating zones. It ceases around 1.7 Gyr when peak central temperatures of about 1015 K are reached; the core then reaches its present-day state, consisting of an inner dry core of radius 290 km and an outer hydrated core of radius 380 km. No melting occurs in this scenario in the absence of antifreezes, as in scenario (b). Liquid convection and hydrothermal circulation are therefore never initiated. As a result, the core is never rehydrated, even as it cools below 700 K. In the hydrosphere, heat is transported by solid state convection of ice, which continues on today, albeit even less vigorously than in scenario (b). Thus, present-day central temperatures (620 K) are the highest of all three scenarios.

5.1.2. Simulations With $\text{NH}_3/\text{H}_2\text{O} = 0.01$ by Mass

Ceres could have accreted ammonia at a level up to 14% with respect to water [Dodson-Robinson *et al.*, 2009]. Subsequently, ammonia may have speciated into ammonium salts [Forte *et al.*, 2007; Marion *et al.*, 2012] or been oxidized to N_2 in hydrothermal reactions [Matson *et al.*, 2007; Glein *et al.*, 2009]. Ammonia could also have reacted with silicates and become integrated into the rock in saponite form; saponite may have been observed on Ceres' surface [King *et al.*, 1992] but this is now contested [Cohen *et al.*, 1998; Rivkin *et al.*, 2006; Milliken and Rivkin, 2009]. Given these uncertainties on the fate of ammonia, we have chosen to investigate its effects for an arbitrary content of 1% by mass (1.06% by mole) with respect to water.

Ammonia does not affect the internal structure of Ceres if present at this level, despite minor differences (e.g., earlier time of differentiation because melting is easier). Ceres' dry inner core, hydrated outer core, and hydrosphere have the same radii as in ammonia-free runs. However, ammonia enables liquid persistence until the present day in the form of a partially molten layer whose mass scales with ammonia content. For a 1% bulk ammonia content in ice, this layer is a few kilometers thick if the melt mass fraction is 70%, but up to 100 km if the melt mass fraction is only 2%, the cutoff for liquid convection in the code. Convection in such a thick, partially molten layer is initiated only in scenario (a) and contributes to cooling Ceres to the point where its present-day central temperature is only 315 K. For the other two scenarios, convection in the liquid is never initiated because early ^{26}Al heating never melts a layer thick enough (the Rayleigh number scales with the cube of the liquid layer thickness). Surprisingly, the presence of liquid does not always lead to hydrothermal circulation, because upper cracked layers may be clogged by mineral precipitation and isolate the cracked layers beneath from the seafloor above (Figures 6d through 6f). Thermal histories are therefore similar to ammonia-free runs (Figure 5).

That hydrothermal circulation may be impeded by mineral precipitation could be a spurious feature of the 1-D code: in practice, precipitation is likely localized in latitude and longitude. Therefore, we have also run the 1% NH_3 scenarios with mineral dissolution and precipitation disabled, in order to investigate the maximum effect of hydrothermal circulation on thermal evolution (Figure 7).

In scenario (a), the entire core is differentiated and cracked in the first Myr, leading to extensive hydrothermal circulation and melting. ^{26}Al heating is sufficient to dehydrate part of the core; however, efficient convective cooling in the outer core and hydrosphere prevents dehydration in a layer 45 km thick. Early rehydration at 45 km depth causes rock to swell and shut off cracks in that layer, preventing the underlying layers from further rehydrating (Figure 6g). Therefore, a structure with an inner dry core of radius 320 km, an outer hydrated core 45 km thick, a partially molten layer (slush) 25 km thick, and an icy crust 85 km thick is established after only 10 Myr and persists to the present day. While the inner core cools by conduction, the outer core and partially molten layer cool primarily by convection. Circulation in the outer core is intermittent, as it is fueled by conductive thermal gradients that it quickly dissipates. This causes the thickness and temperature of the liquid layer to fluctuate slightly (Figure 7a).

Temperature profiles in scenarios (b) and (c) exhibit a curious cyclic behavior, characterized by ~50 Myr intervals during which internal temperatures are cold (below 300 K). These "temperature resets" are caused by episodes of vigorous hydrothermal circulation. Liquid is allowed to circulate through the entire core because core cracks never heal due to insufficient radioactive decay heating, except in the central regions in scenario (c) (Figures 6h and 6i).

Thus, hydrothermal circulation results in efficient heat transfer (occurring by convection, but modeled as enhanced conduction) in both scenarios (b) and (c), cooling down the core and heating up the hydrosphere: only about 50 Myr after circulation is initiated (gray arrows in Figure 7), the temperature profile becomes very shallow. This brief phenomenon almost appears like a series of temperature resets between 0.5 and 3 Gyr in Figures 7b and 7c due to the logarithmic scale for time, but the smooth nature of the temperature changes is more clearly visible in Figure 7b between 10^{-2} and 10^{-1} Gyr. This phenomenon persists as long as hydrothermal circulation operates, i.e., until the thermal gradient becomes shallow enough that the Rayleigh number drops below its critical value of 30 (section 4.2). A steep rise in internal temperatures follows, because of slow conductive heat transfer in hydrated rock. This reheating can cause several subsequent episodes of ice melting and hydrothermal cooling. Past a few Gyr, heating by long-lived radionuclides becomes too weak to initiate new hydrothermal episodes, thus unlikely to occur at the present day or in the near future. In both scenarios, the present-day Ceres is structured into a large hydrated core (radius 410 to 420 km), surrounded by a partially molten layer, itself topped by an icy crust.

5.2. Cracking Model Sensitivity to Free Parameters

The cracking model described above has a number of free or poorly constrained parameters: the fracture toughness K_{IC} , initial subgrid crack width D_i , grain size d , and pore aspect ratio b_p/a_p . We explore the model sensitivity to these parameters.

Crack healing depends on grain size (Figure 3b). Even for grain sizes of 1 μm and strain rates of $(4.56 \text{ Gyr})^{-1}$ that minimize ductile strength, the brittle-ductile transition occurs at radii of 310 km or lower at the highest

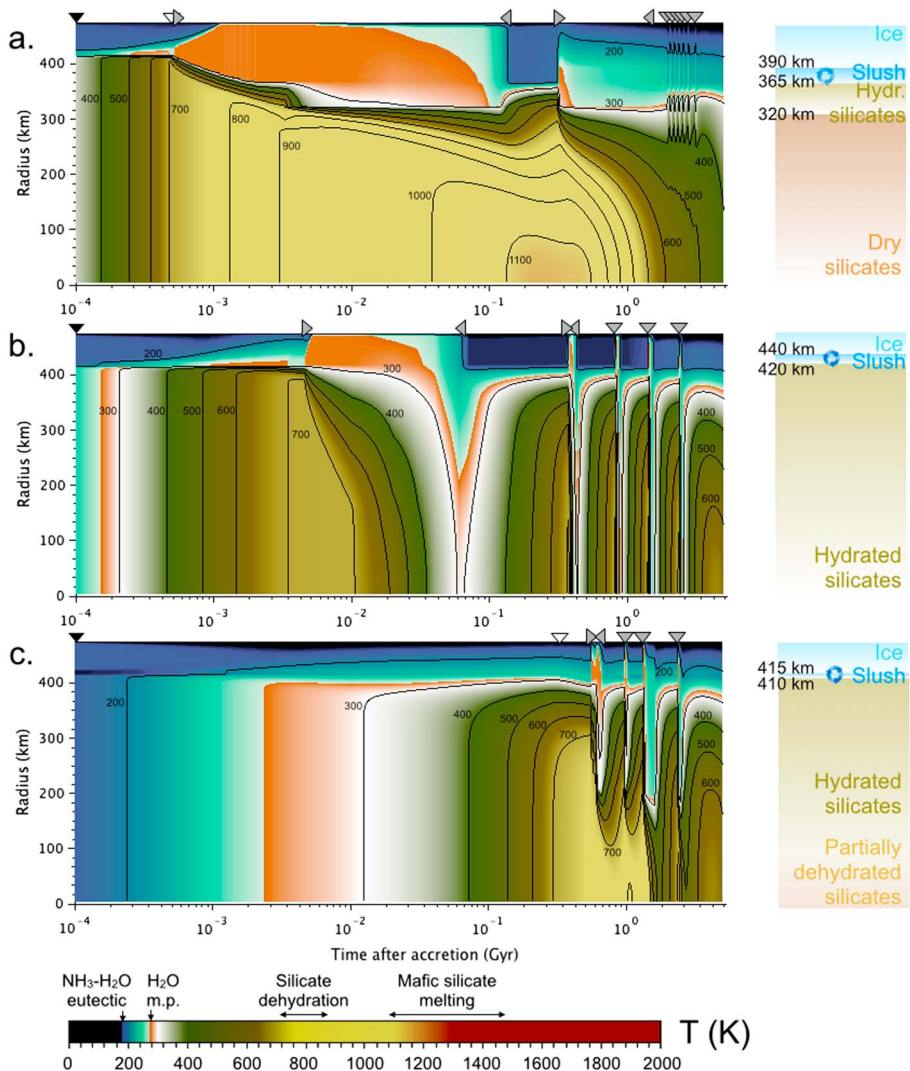


Figure 7. (left) Thermal evolution of Ceres in three cases: accretion (a) 2 Myr, (b) 3 Myr, and (c) 5 Myr after the condensation of Ca-Al inclusions (CAIs). A bulk $\text{NH}_3/\text{H}_2\text{O}$ mass fraction of 10^{-2} is assumed. Black arrows on top of each panel indicate the onset of differentiation. White arrows in Figures 7a and 7c indicate the onset of dehydration, around 700 K (dehydration seldom occurs in scenario (b)). Gray arrows indicate episodes of hydrothermal circulation. (right) Present-day structures of Ceres. Circular arrows indicate convective heat transfer in the corresponding layers. Slush indicates a partially (at least 2%) liquid convective layer.

temperatures experienced. This has little bearing on the structures shown in Figure 5: running scenario (b) with $d = 5 \mu\text{m}$ yields a cracked depth decreased by one grid layer (about 2 km).

Thermal mismatch cracking is more important at shallower core depths where relatively low confining pressures yield the highest K_t . This process may help connect the seafloor to a cracked zone at depth. However, since shallow core regions are already cracked in our simulations, thermal mismatch has no influence on our results. Thermal mismatch cracking is most sensitive to K_{tC} : even the lowest reasonable values of $0.1 \text{ MPa m}^{1/2}$ for hydrated rock and $0.5 \text{ MPa m}^{1/2}$ for dry rock preclude cracking, because K_t is never higher than these values. K_t increases linearly with $\Delta\alpha$, the difference in thermal expansion coefficient between adjacent mineral grains. For olivine, Fredrich and Wong [1986] used $\Delta\alpha = 1.9 \times 10^{-6} \text{ K}^{-1}$ and Vance *et al.* [2007] used $3.1 \times 10^{-6} \text{ K}^{-1}$; but values for $\Delta\alpha$ could be up to $5 \times 10^{-6} \text{ K}^{-1}$, assuming the case of an olivine grain with $\alpha \approx 26.5 \times 10^{-6} \text{ K}^{-1}$ [Osako *et al.*, 2010] surrounded by lizardite grains with $\alpha \approx 32.8 \times 10^{-6} \text{ K}^{-1}$ [Gregorkiewitz *et al.*, 1996]. Such values would yield stress intensities as high as $0.6 \text{ MPa m}^{1/2}$, enough to crack hydrated and, possibly, dry silicates in shallow core regions.

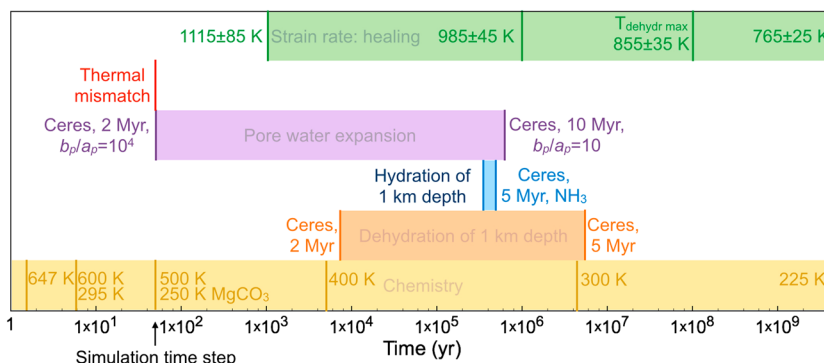


Figure 8. Timescales of cracking processes. Shaded regions show the timescale ranges determined from our simulations. “Ceres, x Myr” denotes the time of accretion, and b_p/a_p denotes the pore aspect ratio. Chemistry timescales assume product activities a_i of 0.

Early core cracking occurs in all scenarios because of heating, which causes silicate dehydration and pore water pressurization. Heating rates are stronger for higher silicate densities. The dehydration cracking equation (16) has no free parameter, but the pore pressurization equation (13) has one: the pore aspect ratio b_p/a_p . Pore pressures are nearly proportional to the aspect ratio for values of b_p/a_p above 10. Pressures accumulate as long as cracking does not occur. They reach values comparable to the confining pressure and silicate brittle strength much faster than the inelastic relaxation time of silicates for the whole range of temperatures for which rock is hydrated ($T < 850$ K). Thus, the pore aspect ratio does not influence whether cracking occurs in our simulations. However, cracking occurs faster for higher values of b_p/a_p , but no later than 3×10^5 years after core differentiation even for $b_p/a_p = 10$ and an accretion time 5 Myr after CAIs, which produce the weakest heating of the scenarios investigated (Figure 8).

Dissolution and precipitation occur in hydrothermal areas. The extent of hydrothermal circulation is increased by a low porosity of the cracked silicates, which decreases the amount of liquid needed for circulation in the fractured layers. The vigor of circulation is also increased, because Ra scales with the circulation depth, even though it also scales with porosity via k_{hydro} in equation (27). Chemical processes are highly dependent on temperature (Figure 8), via both the equilibrium “constant” $K_i(T, P)$ and the Arrhenius term $k_{i\text{diss}}$ for a given reaction (equation 20). Because K_i and $k_{i\text{diss}}$ vary by many orders of magnitude with temperature, free parameters such as initial crack size D_i and area-to-volume ratio A/V do not affect much the fate of cracks. Similarly, hydration and dehydration only have a minor influence on the subgrid crack width D . The high dependence of clogging on temperature makes this process somewhat arbitrary. Clogging does not always happen in adjacent layers, creating at times impermeable layers in the core below which hydrothermal circulation is impeded. Such layering may be a spurious feature of the 1-D code, as precipitation could be localized in latitude and longitude. Discussing the distribution of impermeable precipitates is beyond the scope of our study; but given its potential impact on hydrothermal circulation, this distribution would be worth exploring in further detail with 2-D or 3-D models.

5.3. Timescales of Cracking Processes

5.3.1. Fracture Healing

Cracks heal where rock is ductile. Rock yields by diffusion creep if its ductile strength is lower than its brittle strength. We find brittle strengths and temperatures from 10 MPa and 200 K at Ceres’ seafloor to 200 MPa and 1200 K at its center (Figures 1, 5, and 7). Corresponding strain rates (healing timescales) vary tremendously with temperature, as $\exp(-1/T)$, but only linearly with strength. In Ceres’ core, strain rates range from $(10^3 \text{ yr})^{-1}$ around 1150 K to $(4.6 \text{ Gyr})^{-1}$ around 765 K for grain sizes of 500 μm , increasing by about 3 orders of magnitude for every 200 K increase (Figure 8). These temperatures may shift by up to 100 K depending on brittle strength.

5.3.2. Thermal Mismatch

Thermal mismatch depends on the rate of heating and cooling, i.e., the magnitude of temperature changes estimated over a given timescale. In our simulations, this timescale is the time step, typically 50 years (Figure 8).

5.3.3. Pore Water Pressurization

Pore pressurization timescales range from less than a 50 year time step to 5×10^5 years after differentiation (Figure 8). These timescales depend on early heating rate and pore aspect ratio. The heating rate depends in turn on short-lived radioisotope content (time of accretion), to which the cracking timescale is very sensitive. For an aspect ratio of 10, pore pressurization cracking happens a few thousand years after differentiation if Ceres accretes 2 or 3 Myr after CAIs; but 0.3 to 0.5 Myr for accretion at 5 or 10 Myr after CAIs. Cracking happens first at midcore depths where the combination of heating rate and brittle strength, which both increase with depth, is most favorable.

5.3.4. Core Hydration and Dehydration

The core dehydration front advances 1 km on timescales of 10^4 (Figure 5a) to 5×10^6 years (Figure 5c). The hydration front migrates by 1 km in 4 to 5×10^5 years (Figure 7c). These velocities depend on heating and cooling rates. Dehydration timescales are shorter than those determined by Castillo-Rogez and McCord [2010] by 1 to several orders of magnitude, perhaps because their models assumed early hydration during differentiation; consequently, the heat from ^{26}Al was consumed in melting ice and any residual heat was damped by convection. MacDonald and Fyfe [1985] measured diffusion coefficients of water in serpentinite and inferred that hydration fronts advance by 1 km in $\sim 10^9$ years at room temperature to $\sim 10^6$ years at 573 K. Extrapolating these timescales to the temperatures at which hydration and dehydration take place in our models (700 to 850 K) yields timescales of order 10^5 years, compatible with our findings.

5.3.5. Dissolution and Precipitation

Kinetic chemical processes cover a wide range of timescales, from seconds to over 4.6 Gyr, due to two factors. First, reaction rates vary hugely with temperature, as $\exp(-1/T)$ (Figure 8). Reaction timescales also vary considerably between mineral species, due to differences in activation energies for dissolution. Thus, the dissolution of a crack wall thickness of 1 cm into pure liquid water, estimated using equations (20) through (22), takes about 10^8 years at 250 K for silica or chrysotile, but only 10^3 years for magnesite.

Second, equilibrium constants depend considerably on temperature and pressure. In the ranges 260–1000 K and 1–2500 bar, the equilibrium constants for the dissolution of silica, chrysotile, and magnesite vary by 3.5, 150, and 95 orders of magnitude, respectively, as calculated using the software package CHNOSZ [Dick et al., 2008] with thermodynamic data from Helgeson et al. [1978]. Thus, the timescales shown in Figure 8, where the K_i play no role, can be profoundly modified for nonzero product activities if equilibrium dominates kinetics. In practice, two cases may occur. First, timescales may be such that some dissolution occurs during a time step. In this case, activities are usually high enough that precipitation and clogging will likely occur at a later time step. Second, the timescale for mineral dissolution and precipitation can be much shorter than the simulation time step. In this case, cracks are not affected because everything that dissolves during a time step also precipitates back: crack width changes ΔD , in equations (21) and (22) are equal. Thus, when chemical processes occur on timescales too different from the ranges of other processes displayed in Figure 8, they do not affect cracking in the model.

5.4. Material Compressibility

In our simulations, in which volume changes are forbidden, we have implicitly assumed that the compressibility of rocky and icy materials can be neglected. To verify this assumption, we have computed the effect of material compression on density and pressure profiles inside Ceres generated by the thermal evolution code at 4.56 Gyr. Using these input profiles, we have solved the third-order Birch-Murnaghan equation of state [Birch, 1947] for silicates [Chung, 1971; Auzende et al., 2006] and ammonia dihydrate ice [Fortes et al., 2003], as well as a pressure-dependent equation of state for liquid water and ice Ih [Choukroun and Grasset, 2010], to generate output profiles accounting for material compression.

The compacted density profiles do not differ much from those that neglect compression: the radii of the inner dry core, outer hydrated core, and ice shell differ by less than 10 km in all scenarios. Pressures differ by less than 15%, with the largest discrepancies at the center. These results support a posteriori our assumptions that Ceres' interior experiences little compression. Errors arising by not accounting for compression are less than those linked to the assumption that Ceres is spherically symmetric, since Ceres' short and long axes have radii that differ by about 40 km [Drummond et al., 2014].

5.5. Heat Sources

In all scenarios, most of the heat budget is contributed by long-lived radionuclides, which produce 2 orders of magnitude more cumulated heat than the release of potential energy. Short- and long-lived

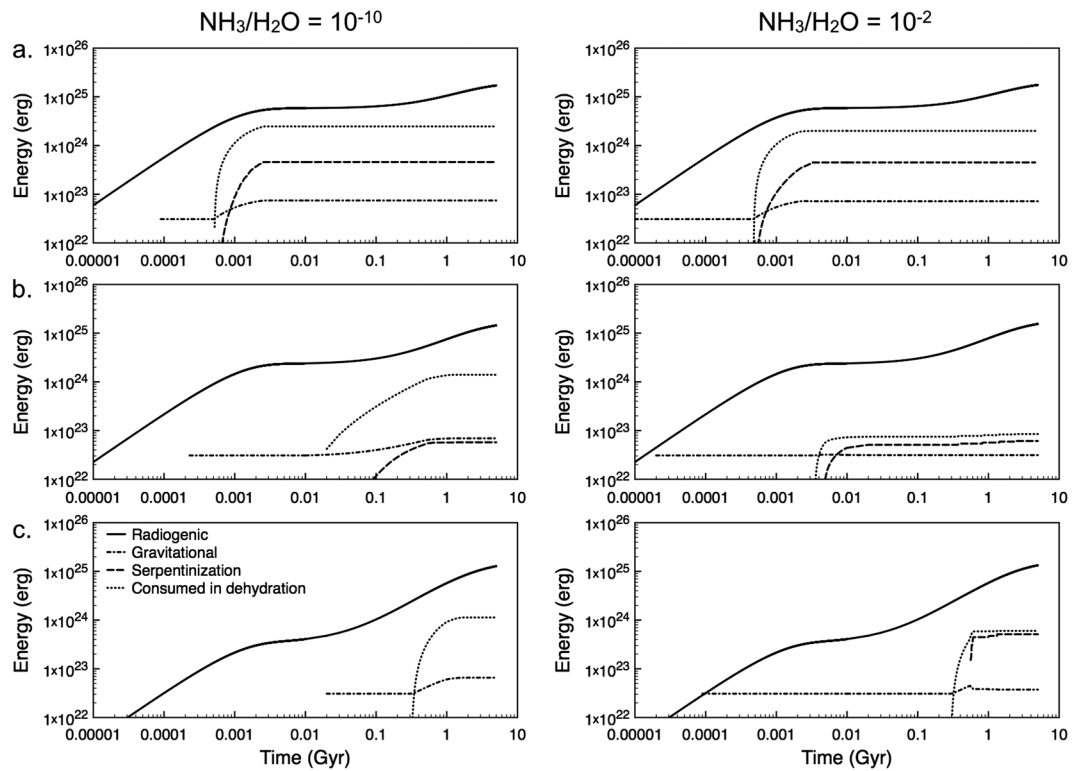


Figure 9. Cumulated radiogenic, serpentinization (silicate hydration), and gravitational heating of Ceres through time in three scenarios: accretion (a) 2 Myr, (b) 3 Myr, and (c) 5 Myr after the condensation of Ca-Al inclusions (CAIs). Results are shown for simulations with $\text{NH}_3/\text{H}_2\text{O}$ by mass of 10^{-10} (left) and 10^{-2} (right). Heat consumption by silicate dehydration is also plotted.

radionuclide heating can be seen in Figure 9 as separate increases in heat produced. ^{26}Al decay heating dominates the cumulative heat budgets in all scenarios for the first 10 Myr. Gravitational heating occurs during differentiation and core dehydration.

Serpentinization is not a significant heat source. This could be due to a lack of either fractures (scenario (a)) or liquid (scenarios (b) and (c) with negligible NH_3); however, even when both persist over geological timescales, radiogenic heating still dominates (scenario (c) with 1% NH_3). Interestingly, serpentinization heating is most prominent in scenario (a) for which Ceres' core is most dehydrated (Figure 9). This is because hydrothermal circulation is pervasive early on during dehydration, which is slowed down by partial rehydration due to circulating fluids. Dehydration is a significant heat sink in almost all scenarios and contributes to keeping Ceres' core from reaching melting temperatures.

Locally, hydration and dehydration can lead to changes in heat content 2 orders of magnitude higher than those caused by radioactivity. Gravitational heating due to contraction of silicate layers from dehydration is locally only an order of magnitude lower than radiogenic heating.

6. Discussion

6.1. Comparison With Results of Previous Studies

6.1.1. Core Cracking Models of Vance et al. [2007]

To our knowledge, only *Vance et al. [2007]* have modeled cracking in the cores of icy worlds. They assumed that cracks develop in a dry rocky core by thermal contraction mismatch. Structures for most bodies were provided by the steady state models of *Hussmann et al. [2006]*. *Vance et al. [2007]* assumed present-day cooling rates of 1 K yr^{-1} to 1 K Gyr^{-1} , and grain sizes of 0.1 to 10 mm. For a cooling rate of 1 K yr^{-1} , a grain size of 1 mm, and $K_{IC} = 0.6 \text{ MPa m}^{1/2}$, they predicted that bodies the size of Enceladus (radius 250 km) to Oberon (radius 760 km) may experience core cracking depths of 100 to 170 km. These depths were doubled for a tenfold increase in grain size and were fourfold lower for cooling rates of 1 K Gyr^{-1} . Their results suggested that the core of Ceres-sized bodies may be entirely cracked [*Castillo-Rogez and McCord, 2010*].

We suggest that thermal mismatch plays little role in cracking Ceres' core. Cooling rates are of order 10 K Gyr^{-1} at the present day in outer core layers, at the lower end of the range assumed by *Vance et al.* [2007]. Assuming such a cooling rate, a grain size of $500 \mu\text{m}$, and all other parameter values equal to those in their study ($E = 197 \text{ GPa}$, $K_{IC} = 0.6 \text{ MPa m}^{1/2}$), we do find thermal mismatch cracking depths in dry silicate of 5 to 20 km. However, our simulations show that the upper core is more likely hydrated, in which case silicate Young moduli E are as low as 35 GPa [*Christensen*, 1966; *Hirth and Kohlstedt*, 1995]. This sixfold decrease in E is enough to prevent thermal mismatch cracking in our models.

6.1.2. Models of McCord and Sotin [2005]

McCord and Sotin [2005] studied the thermal evolution of Ceres for two scenarios: undifferentiated and differentiated. They concluded that Ceres must have differentiated into a rocky core and an icy mantle, with little internal porosity. We support these conclusions. They also suggested that the core may be entirely hydrated, in which case Ceres would cool faster (by conduction through a thinner ice shell) than with a dry silicate core. We show that cooling actually seems to occur mainly by convective heat transport through the upper core and hydrosphere. *McCord and Sotin* [2005] did not predict iron-silicate differentiation since internal temperatures did not exceed 900 K in their models. Melting experiments on fragments of the Allende carbonaceous chondrite, a possible analog to Ceres' primordial rocky material, suggest that temperatures above 1400 K would be required [*Agee et al.*, 1995]. Such temperatures are not reached in our simulations either. *McCord and Sotin* [2005] pointed out that a metal core may form if accretional heating produces the temperatures needed; we consider this unlikely, especially since many past estimates of accretional heating have assumed accretion from heliocentric impactors [*Safronov*, 1978], a model now obsolete.

6.1.3. Models of Castillo-Rogez and McCord [2010]

Castillo-Rogez and McCord [2010] investigated scenarios similar to those explored here. They suggested that hydrothermal circulation, along with the time of formation, could be a major evolution driver; however, they did not explicitly model hydrothermal processes. We show here that hydrothermal activity could persist in the outer core over geological timescales due to long-lived cracking in the rocky core, not just during early evolution as they suggested. Heat is thus transferred out of the core and keeps the hydrosphere melted. This in turn favors heat loss by vigorous convective heat transfer, resulting in lower present-day core and hydrosphere temperatures than in their models.

Another impact of hydrothermal circulation expected by *Castillo-Rogez and McCord* [2010] was rock hydration, which results in heat production, volume changes, and decreased rock thermal conductivity. All these phenomena occur if conditions for circulation are favorable: high NH_3 content, highly fractured core (no dehydration), and little mineral precipitation. If so, the impact on Ceres' thermal evolution is significant (Figure 7). Otherwise, hydrothermal effects are small (Figure 5) because late hydration is prevented for three reasons. First, there may not be enough liquid. Second, thermal contraction mismatch, the only core cracking process in cooling regions, is ineffective. Third, even cracks that open before cooling starts, and do not heal, can be clogged by precipitated minerals.

6.1.4. Models of Malamud and Prialnik [2015]

Malamud and Prialnik [2015] modeled the thermal evolution of the Ceres-sized Kuiper belt object Orcus (radius 459 km) with a level of detail similar to that presented here, including serpentinization. When comparing simulation outcomes, one must bear in mind a few differences. First, the bulk density of Orcus is only 1530 kg m^{-3} , implying a rock/ice mass ratio of 3 (with their chosen densities), twice as low as that we derive for Ceres (6.25). Second, the surface temperature of Orcus is only 41 K, assuming the albedo value used by *Malamud and Prialnik* [2015]. Third, ^{26}Al heating is likely negligible at the accretion timescales of the Kuiper belt, of order 10^7 years [*Kenyon and Bromley*, 2012]. Finally, silicate-ice differentiation is very gradual in the models of *Malamud and Prialnik* [2015], proceeding as the diffusion of ice and volatiles through a rock matrix. In the present code, differentiation occurs when the temperature of a given layer exceeds a threshold; every layer below is rearranged instantaneously into a core and mantle.

Despite these differences, some modeling results of *Malamud and Prialnik* [2015] for Orcus are similar to our scenario (c) with negligible NH_3 . Orcus' present-day central temperature is 550 K (620 K for Ceres). The temperature gradient is steeper in Orcus' core, due to a colder ice-rich shell and slow conductive heat transport through the highly porous outer core. The peak temperature reached inside Orcus is 890 K around 2 Gyr after formation; Ceres reaches 1015 K around 1.6 Gyr. *Malamud and Prialnik* [2015] do not allow for silicate dehydration; therefore, Orcus' core remains hydrated throughout their simulation. The outer core, which

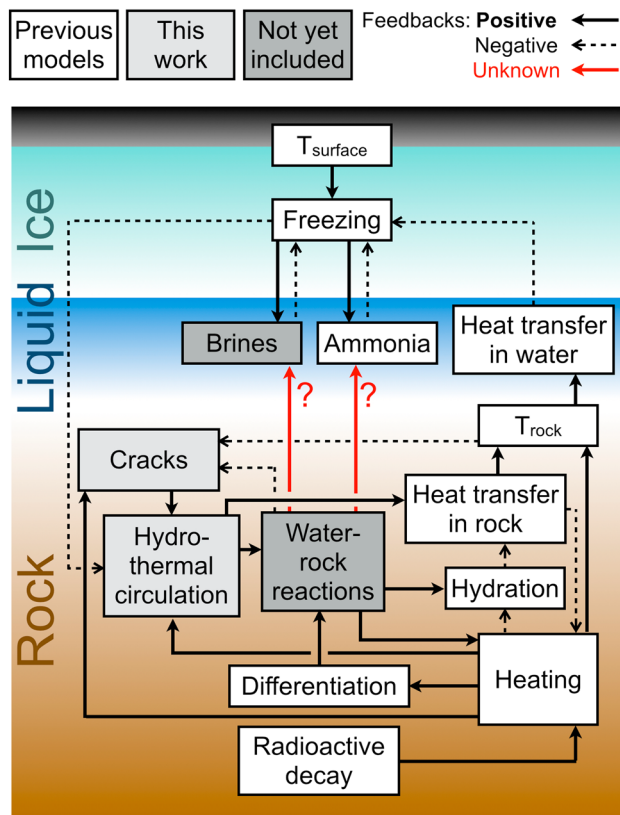


Figure 10. The inclusion of core cracking and hydrothermal circulation in evolution models of Ceres (light gray boxes) enables the investigation of key feedback loops in endogenic processes. Such loops were suggested, but not explicitly modeled, in previous work [McCord and Sotin, 2005; Castillo-Rogez and McCord, 2010]. A full understanding of the coupled geophysical-geochemical evolution of Ceres will require investigation of the fate of ammonia and brine antifreezes, as well as the possibility of radionuclide leaching via water-rock reactions [Castillo-Rogez and Lunine, 2010] (dark gray boxes).

core dehydration, but hindered by high core temperatures and by precipitates of leaches resulting from water-rock interactions. Cracking seems insensitive to hydration swelling of rock.

Liquid can be generated not only by melting ice but also by dehydrating silicates. The relative importance of each source depends on the extent of core dehydration. Up to 60% of the long-lasting liquid originates from dehydration in scenario (a), with or without NH_3 antifreeze. In scenarios (b) and (c) with negligible NH_3 , any liquid originating in core dehydration is refrozen in 10 Myr or less; with 1% NH_3 , little or no dehydration occurs and all present-day liquid originates in melting ice.

Provided liquid persists, core cracking can greatly speed up heat transfer out of the core and into the hydrosphere, due to hydrothermal circulation in the fractured zone (Figure 7). Hydrothermal circulation and ocean convection are tightly linked, because hydrothermalism warms the ocean, which in turn provides liquid to circulate. An unintuitive consequence of convective heat transfer on Ceres' evolution is that a hotter birth seems to lead to a cooler present state. However, strong hydrothermal heat transfer is eventually self-limiting as it both smoothes out the thermal gradients by which it is fueled and causes liquid to refreeze. In Figure 10, this is shown by two negative feedback loops. A first loop links hydrothermal circulation, heat transfer in rock, and heating. A second loop links hydrothermal circulation, heat transfer in rock, rock temperature, heat transfer in water, and freezing.

Finally, the extent of cracking determines that of water-rock interactions. Surprisingly, these often seem to result in crack clogging in the present model, preventing further interaction. The possibility of such an

spans radii of 200 km to 350 km, is highly porous; Ceres' cracked zone spans radii from 290 km to 380 km. Thus, the volumes of fractured or porous rock are very similar. Malamud and Prialnik [2015] found Orcus' ice shell to be highly porous, which is reasonable at frigid near-surface temperatures; on Ceres, the porosity is likely negligible except in the surface regolith [McCord and Sotin, 2005].

Serpentinization is a major heat source in the model of Malamud and Prialnik [2015], which assumes silicates to be initially dehydrated. A hydration heat pulse is released after about 200 Myr as differentiation occurs in their simulation. This pulse seems to exceed radiogenic heating for a brief period, releasing about a tenth of the long-lived radiogenic heat produced over 4.6 Gyr. In our models, serpentinization is usually less prominent, perhaps because hydrothermal circulation is more efficient at removing that heat.

6.2. Geophysical and Geochemical Feedbacks

Our models of core cracking make the essential link between geophysical and geochemical processes, elucidating some feedbacks shown in Figure 10. Crack formation is favored by high heating or cooling rates and

inhibiting effect was noted by *McKinnon and Zolensky* [2003]. However, more detailed and faithful chemical modeling is needed to explore water-rock reaction outcomes. Unknown consequences on the distribution of solute antifreezes and radionuclides remain to be investigated (Figure 10). Follow-up geochemical calculations are likely to use water to rock ratios as an input. Our simulations suggest bulk mass ratios (mass of liquid/mass of cracked rock, assuming all the liquid is circulated) between 0.005 and 0.015 when hydrothermal circulation occurs through a large portion of the core (all 1% NH₃/H₂O cases), and between 0.1 and 5 if water is circulated only in a few upper core layers (scenario (a) with negligible NH₃).

6.3. Testing Predictions With Dawn Observations

6.3.1. Gravity Measurements

Two parameters of Ceres' internal structure seem key to understanding its origin. The first is the core size, which seems to depend on Ceres' time of formation. In the absence of late hydration, the final core size is set by the extent of silicate dehydration, which in turn depends on the amount of ²⁶Al heating in our simulations. The long-term evolution of the core may be further affected by leaching of the ⁴⁰K in water-rock reactions, taking away part of the core's radiogenic fuel [*Castillo-Rogez and McCord*, 2010]. Core sizes of 370 km or less may suggest both an early time of formation near Ceres' current heliocentric distance, and little hydrothermal activity. The second parameter is the amount of liquid involved in crack circulation, directly proportional to antifreeze content in our calculations. In turn, the amount of volatile antifreezes accreted depends on Ceres' place of formation, with larger amounts accreted if Ceres formed further away from the Sun [*Dodson-Robinson et al.*, 2009]. However, salt compounds leached from silicates during hydrothermal alteration may also act as antifreeze; this remains to be explored.

Constraints on the internal structure of Ceres will be obtained by gravimetry via Doppler tracking of the *Dawn* spacecraft. Ceres' bulk density and gravitational moment J_2 should be measured to respectively 1% and 0.001% [*Russell and Raymond*, 2011; *Russell et al.*, 2012]; to the extent that the assumption of hydrostatic equilibrium can be applied to Ceres, the measurement of J_2 may provide an estimate of its moment of inertia. Similar constraints on the internal structures of Titan and Enceladus have recently been obtained by tracking of the *Cassini* orbiter [*Iess et al.*, 2012, 2014]. The gravitational signature of a liquid layer inside Ceres may be difficult to detect if this layer also contains substantial amounts of water ice and ammonia. Evidence for subsurface liquid could have been collected with a magnetometer able to detect an induced field on Ceres due to salt water. Unfortunately, *Dawn*'s magnetometer was descoped [*Russell and Raymond*, 2011].

6.3.2. Compositional Mapping

Finer constraints on Ceres' evolution may be obtained by inferring the temperature and pressure at which formed the surface carbonates and clays, likely products of aqueous alteration [*Milliken and Rivkin*, 2009]. Our results suggest two possible settings. First, hydrated minerals form early on during differentiation, or perhaps even in the primordial bodies accreted by Ceres [*Zolotov*, 2014]. Water-rock interaction products are circulated upwards into the ocean, then brought to the surface by ice convection. Second, hydrated minerals are formed in the cracked outer core layers experiencing hydrothermal circulation as late as 3 Gyr after Ceres' formation, then brought to the surface by ice convection.

Discriminating between these scenarios requires age estimates of the surface deposits. Estimates may be obtained using spectra acquired by *Dawn*'s Visible and InfraRed spectrometer (VIR) instrument [*De Sanctis et al.*, 2011, 2012], imaging by *Dawn*'s Framing Camera [*Sierks et al.*, 2011], and models of crater relaxation [*Bland*, 2013; *Dombard and Schenk*, 2013].

Timing, physical, and chemical constraints on the fluid-rock reactions that formed Ceres' surface minerals could be obtained with geochemical speciation or reaction path models coupled to a geophysical code. Such modeling could allow interpretation of compositional measurements in terms of constraints on Ceres' evolution and present state. Spectral observations of Ceres' surface at high spatial resolution may allow pinpointing of local heterogeneities from current global averages, which may have hindered previous interpretations of spectra. More complex or yet unidentified species may be detected. For example, the current absence of salts in spectra of Ceres [*Zolotov*, 2014] does not preclude their existence on the surface: salts are harder to detect than hydrated minerals, because higher degrees of hydration yield shallower reflectance features [*McCord et al.*, 2002; *De Sanctis et al.*, 2012]. Infrared remote sensing probes a depth of only a few wavelengths, bringing about the need to discriminate between an endogenic or exogenic source of the materials observed. *Dawn*'s Gamma Ray and Neutron Detector (*GRaND*) [*Prettyman et al.*, 2011] will

help with this issue. *GRaND*'s objective is to map abundances of major rock-forming elements (O, Na, Mg, Al, Si, K, Ca, and Fe) to 20% precision at a resolution of 1.5 times the mapping altitude, within a depth of order 1 m. Salt-forming elements P, S, and Cl may also be observed. Correlations between *VIR* and *GRaND* measurements will establish the contribution of endogenic materials in *VIR* spectra.

6.3.3. Possible Cryovolcanic Activity

Küppers *et al.* [2014] recently reported observations of water vapor expelled from Ceres. The vapor sources seem both spatially and temporally confined. Whether these sources arise from sublimation of near-surface ice or from cryovolcanism is unknown. Cryovolcanism may be favored by freezing, which could pressurize liquid water reservoirs [Fisher, 2003; Neveu *et al.*, 2015]. Our results suggest that under certain conditions (late accretion, presence of antifreezes) it might be possible for Ceres to undergo global freezing at the present day (Figures 7b and 7c). Even if Ceres' interior is currently frozen and the current activity is not cryovolcanic, Ceres' surface might show evidence of periodic cryovolcanism over geologic time, which could be linked to the ending of the periodic hydrothermal episodes suggested by some of our simulations.

7. Conclusions

We have described new geophysical evolution models for icy dwarf planets, applied to Ceres, that focus on core cracking and hydrothermal circulation. The models account for the following fracturing processes: brittle-ductile transition in dry and hydrated rock, thermal mismatch of mineral grains, thermal pressurization of pores, silicate swelling and shrinking upon hydration and dehydration, and mineral dissolution and precipitation.

We have found that the depth of the fractured zone depends mainly on peak core temperatures. While the entire core is initially cracked due to either pore pressurization or dehydration shrinking stresses, only core layers that never experience temperatures higher than about 800 K remain fractured on geological timescales; otherwise, cracks heal from the ductile creep of silicates. It is unlikely that core cracking occurs as Ceres cools, because thermal contraction mismatch seems ineffective at fracturing silicates. Present-day cracked depths, of 5 to 420 km in our simulations, suggest a significant volume of rock available to interact with liquid, if present.

The presence of liquid hinges on antifreeze content, on silicate dehydration (which releases liquid), and on hydrothermal circulation itself (which efficiently transports core heat into the hydrosphere). The heat of serpentinization seems too small to significantly help liquid persist.

If liquid persisted over geological timescales, hydrothermal circulation may have profoundly affected Ceres' thermal and geophysical evolution. If shallow, hydrothermal circulation helped sustain liquid by efficiency tapping the core's heat, yet not cooling the core too quickly. If reaching deep into the core, hydrothermal circulation may have prevented core dehydration through temperature resets, global cooling events lasting about 50 Myr during which Ceres' interior temperature profile was very shallow and the hydrosphere was largely melted.

Hydrothermalism may have left its mark on Ceres' present-day structure. A large, fully hydrated core (radius 420 km) suggests that extensive hydrothermal circulation prevented core dehydration. A small, dry core (radius 350 km) suggests early dehydration from short-lived radionuclides, with shallow hydrothermalism at best. Intermediate structures with a partially dehydrated core seem more ambiguous, being compatible both with late partial dehydration without hydrothermal circulation, and with early dehydration with extensive hydrothermalism. While current shape data do not allow discrimination between these possible structures [Castillo-Rogez and McCord, 2010], gravity measurements by the *Dawn* mission may.

As a final note, our estimates of the cracking depth constrain not only the extent of water-rock interactions but also the potential of icy dwarf planets to support the emergence and persistence of chemotrophic microbes [Vance *et al.*, 2007]. The habitability of subseafloor hydrothermal areas depends on their elemental inventory and the speciation of these elements, as well as on the amount of chemical energy available. Possible hydrothermal chemistries inside Ceres and other icy dwarf planets will be the topic of a future paper.

Acknowledgments

We thank Everett Shock for discussions on cracking phenomena that helped improve this paper. Comments from two referees and the Associate Editor greatly helped improve this manuscript. This study was funded by the NASA Astrobiology Institute team at Arizona State University and by the NASA Outer Planets Research and Earth and Space Science Fellowship programs. Part of this work has been carried out at the Keck Institute for Space Studies and at the Jet Propulsion Laboratory, California Institute of Technology. The code used in this study is freely available at <https://github.com/MarcNeveu/IcyDwarf>.

References

- Abramov, O., and D. A. Kring (2005), Impact-induced hydrothermal activity on early Mars, *J. Geophys. Res.*, 110, E12S09, doi:10.1029/2005JE002453.
- Agee, C., J. Li, M. Shannon, and S. Circone (1995), Pressure-temperature phase diagram for the Allende meteorite, *J. Geophys. Res.*, 100(B9), 17,725–17,740.
- Auzende, A.-L., R.-M. Pellenq, B. Devouard, A. Baronnet, and O. Grauby (2006), Atomistic calculations of structural and elastic properties of serpentine minerals: The case of lizardite, *Phys. Chem. Miner.*, 33(4), 266–275.
- Backers, T. (2005), Fracture toughness determination and micromechanics of rock under mode I and mode II loading, PhD dissertation, Univ. of Potsdam, Germany.
- Bales, R. C., and J. J. Morgan (1985), Dissolution kinetics of chrysotile at pH 7 to 10, *Geochim. Cosmochim. Acta*, 49(11), 2281–2288.
- Balme, M., V. Rocchi, C. Jones, P. Sammonds, P. Meredith, and S. Boon (2004), Fracture toughness measurements on igneous rocks using a high-pressure, high-temperature rock fracture mechanics cell, *J. Volcanol. Geotherm. Res.*, 132(2), 159–172.
- Barnhart, C., F. Nimmo, and B. Travis (2010), Martian post-impact hydrothermal systems incorporating freezing, *Icarus*, 208(1), 101–117.
- Birch, F. (1947), Finite elastic strain of cubic crystals, *Phys. Rev.*, 71(11), 809.
- Bizzarri, A., and M. Cocco (2006), A thermal pressurization model for the spontaneous dynamic rupture propagation on a three-dimensional fault: 1. Methodological approach, *J. Geophys. Res.*, 111, B05303, doi:10.1029/2005JB003862.
- Bland, M. T. (2013), Predicted crater morphologies on Ceres: Probing internal structure and evolution, *Icarus*, 226(1), 510–521.
- Bolton, E. W., A. C. Lasaga, and D. M. Rye (1997), Dissolution and precipitation via forced-flux injection in a porous medium with spatially variable permeability: Kinetic control in two dimensions, *J. Geophys. Res.*, 102(B6), 12,159–12,171.
- Bolton, E. W., A. C. Lasaga, and D. M. Rye (1999), Long-term flow/chemistry feedback in a porous medium with heterogeneous permeability: kinetic control of dissolution and precipitation, *Am. J. Sci.*, 299(1), 1–68.
- Boudier, F., A. Baronnet, and D. Mainprice (2010), Serpentinite mineral replacements of natural olivine and their seismic implications: Oceanic lizardite versus subduction-related antigorite, *J. Petrol.*, 51(1–2), 495–512.
- Bouhifd, M., D. Andrault, G. Fiquet, and P. Richet (1996), Thermal expansion of forsterite up to the melting point, *Geophys. Res. Lett.*, 23(10), 1143–1146.
- Bowling, T., B. Johnson, D. Blair, and J. Melosh (2014), Large impact basins on ceres: Probing beneath the icy mantle, Abstract P41E-03 presented at 2014 AGU Fall Meeting, AGU, San Francisco, Calif.
- Brace, W., and D. Kohlstedt (1980), Limits on lithospheric stress imposed by laboratory experiments, *J. Geophys. Res.*, 85(B11), 6248–6252.
- Byerlee, J. (1978), Friction of rocks, *Pure Appl. Geophys.*, 116(4–5), 615–626.
- Carry, B., C. Dumas, M. Fulchignoni, W. J. Merline, J. Berthier, D. Hestroffer, T. Fusco, and P. Tamblyn (2008), Near-infrared mapping and physical properties of the dwarf-planet Ceres, *A&A*, 478(1), 235–244, doi:10.1051/0004-6361:20078166.
- Castillo-Rogez, J. C., and J. I. Lunine (2010), Evolution of Titan's rocky core constrained by Cassini observations, *Geophys. Res. Lett.*, 37, L20205, doi:10.1029/2010GL044398.
- Castillo-Rogez, J. C., and T. B. McCord (2010), Ceres' evolution and present state constrained by shape data, *Icarus*, 205(2), 443–459, doi:10.1016/j.icarus.2009.04.008.
- Castillo-Rogez, J. C., D. L. Matson, C. Sotin, T. V. Johnson, J. I. Lunine, and P. C. Thomas (2007), Iapetus' geophysics: Rotation rate, shape, and equatorial ridge, *Icarus*, 190, 179–202, doi:10.1016/j.icarus.2007.02.018.
- Castillo-Rogez, J. C., T. V. Johnson, M. H. Lee, N. J. Turner, D. M. Matson, and J. I. Lunine (2010), 26Al decay: Heat production and a revised age for Iapetus, *Icarus*, 204(2), 658–662, doi:10.1016/j.icarus.2009.07.025.
- Cherkaoui, A. S., and W. S. Wilcock (2001), Laboratory studies of high Rayleigh number circulation in an open-top Hele-Shaw cell: An analog to mid-ocean ridge hydrothermal systems, *J. Geophys. Res.*, 106(B6), 10,983–11,000.
- Choukroun, M., and O. Grasset (2010), Thermodynamic data and modeling of the water and ammonia-water phase diagrams up to 2.2 GPa for planetary geophysics, *J. Chem. Phys.*, 133(14), 144502.
- Christensen, N. I. (1966), Elasticity of ultrabasic rocks, *J. Geophys. Res.*, 71(24), 5921–5931.
- Christensen, N. I. (1996), Poisson's ratio and crustal seismology, *J. Geophys. Res.*, 101(B2), 3139–3156.
- Chung, D. (1971), Elasticity and equations of state of olivines in the Mg₂SiO₄-Fe₂SiO₄ system, *Geophys. J. Int.*, 25(5), 511–538.
- Clauzer, C., and E. Huenges (1995), Thermal conductivity of rocks and minerals, in *Rock Physics and Phase Relations: A Handbook of Physical Constants*, vol. 3, edited by T. J. Ahrens, pp. 105–126, AGU, Washington, D. C.
- Cohen, B. A., and R. F. Coker (2000), Modeling of liquid water on CM meteorite parent bodies and implications for amino acid racemization, *Icarus*, 145(2), 369–381.
- Cohen, M., F. C. Witteborn, T. Roush, J. Bregman, and D. Wooden (1998), Spectral irradiance calibration in the infrared. VIII. 5–14 micron spectroscopy of the asteroids Ceres, Vesta, and Pallas, *Astron. J.*, 115(4), 1671.
- De Sanctis, M., et al. (2011), The VIR spectrometer, *Space Sci. Rev.*, 163, 329–369, doi:10.1007/s11214-010-9668-5.
- De Sanctis, M. C., et al. (2012), Detection of widespread hydrated materials on Vesta by the VIR imaging spectrometer on board the Dawn mission, *Astrophys. J. Lett.*, 758(2), L36.
- DeMartin, B., G. Hirth, and B. Evans (2004), Experimental constraints on thermal cracking of peridotite at oceanic spreading centers, in *Mid-Ocean Ridges*, edited by C. R. German, J. Lin, and L. M. Parson, pp. 167–185, AGU, Washington, D. C.
- Desch, S. J., J. C. Cook, T. Doggett, and S. B. Porter (2009), Thermal evolution of Kuiper belt objects, with implications for cryovolcanism, *Icarus*, 202(2), 694–714, doi:10.1016/j.icarus.2009.03.009.
- Dick, J. M., et al. (2008), Calculation of the relative metastabilities of proteins using the CHNOSZ software package, *Geochem. Trans.*, 9, 10.
- Dodson-Robinson, S. E., K. Willacy, P. Bodenheimer, N. J. Turner, and C. A. Beichman (2009), Ice lines, planetesimal composition and solid surface density in the solar nebula, *Icarus*, 200(2), 672–693.
- Dombard, A., and P. Schenk (2013), The giant cue ball: Efficient relaxation of Ceres' craters, Abstracts 1798 paper presented at 44th Lunar and Planetary Institute Science Conference.
- Drummond, J., and J. Christou (2008), Triaxial ellipsoid dimensions and rotational poles of seven asteroids from Lick Observatory adaptive optics images, and of Ceres, *Icarus*, 197(2), 480–496.
- Drummond, J., B. Carry, W. Merline, C. Dumas, H. Hammel, S. Erard, A. Conrad, P. Tamblyn, and C. Chapman (2014), Dwarf planet Ceres: Ellipsoid dimensions and rotational pole from Keck and VLT adaptive optics images, *Icarus*, 236, 28–37.
- Dutrow, B., and D. Norton (1995), Evolution of fluid pressure and fracture propagation during contact metamorphism, *J. Metamorph. Geol.*, 13(6), 677–686.
- Ellsworth, K., and G. Schubert (1983), Saturn's icy satellites: Thermal and structural models, *Icarus*, 54(3), 490–510.
- Escartín, J., G. Hirth, and B. Evans (1997a), Effects of serpentinization on the lithospheric strength and the style of normal faulting at slow-spreading ridges, *Earth Planet. Sci. Lett.*, 151(3), 181–189.

- Escartin, J., G. Hirth, and B. Evans (1997b), Nondilatant brittle deformation of serpentinites: Implications for Mohr-Coulomb theory and the strength of faults, *J. Geophys. Res.*, 102(B2), 2897–2913.
- Escartin, J., G. Hirth, and B. Evans (2001), Strength of slightly serpentinized peridotites: Implications for the tectonics of oceanic lithosphere, *Geology*, 29(11), 1023–1026.
- Evans, A., and D. Clarke (1980), Residual stresses and microcracking induced by thermal contraction inhomogeneity, in *Thermal Stresses in Severe Environments*, edited by D. P. H. Hasselman and R. A. Heller, pp. 629–648, Springer, New York.
- Evans, B. W., K. Hattori, and A. Baronnet (2013), Serpentinite: What, why, where?, *Elements*, 9(2), 99–106.
- Fisher, A. T. (1998), Permeability within basaltic oceanic crust, *Rev. Geophys.*, 36, 143–182, doi:10.1029/97RG02916.
- Fisher, A. T. (2003), Considerations for effusive cryovolcanism on Europa: The post-Galileo perspective, *J. Geophys. Res.*, 108(E12), 5139, doi:10.1029/2003JE002128.
- Fortes, A., I. Wood, J. Brodholt, and L. Vočadlo (2003), The structure, ordering and equation of state of ammonia dihydrate ($\text{NH}_3 \cdot 2\text{H}_2\text{O}$), *Icarus*, 162(1), 59–73.
- Fortes, A., P. Grindrod, S. Trickett, and L. Vočadlo (2007), Ammonium sulfate on Titan: Possible origin and role in cryovolcanism, *Icarus*, 188(1), 139–153.
- Fredrich, J. T., and T.-F. Wong (1986), Micromechanics of thermally induced cracking in three crustal rocks, *J. Geophys. Res.*, 91(B12), 12,743–12,764.
- Funatsu, T., M. Seto, H. Shimada, K. Matsui, and M. Kuruppu (2004), Combined effects of increasing temperature and confining pressure on the fracture toughness of clay bearing rocks, *Int. J. Rock Mech. Min. Sci.*, 41(6), 927–938.
- Germanovich, L. N., R. P. Lowell, and D. K. Astakhov (2001), Temperature-dependent permeability and bifurcations in hydrothermal flow, *J. Geophys. Res.*, 106(B1), 473–495.
- Glein, C. R., S. J. Desch, and E. L. Shock (2009), The absence of endogenic methane on Titan and its implications for the origin of atmospheric nitrogen, *Icarus*, 204(2), 637–644, doi:10.1016/j.icarus.2009.06.020.
- Goldfarb, M. S., and J. R. Delaney (1988), Response of two-phase fluids to fracture configurations within submarine hydrothermal systems, *J. Geophys. Res.*, 93(B5), 4585–4594.
- Goodman, J. C., and E. Lenferink (2012), Numerical simulations of marine hydrothermal plumes for Europa and other icy worlds, *Icarus*, 221(2), 970–983.
- Gregorkiewitz, M., B. Lebech, M. Mellini, and C. Viti (1996), Hydrogen positions and thermal expansion in lizardite-1 T from Elba: A low-temperature study using Rietveld refinement of neutron diffraction data, *Am. Mineral.*, 81(9), 1111–1116.
- Griffith, A. A. (1921), The phenomena of rupture and flow in solids, *Philos. Trans. R. Soc. London, Ser. A*, 221, 163–198.
- Grimm, R. E., and H. Y. McSween (1989), Water and the thermal evolution of carbonaceous chondrite parent bodies, *Icarus*, 82(2), 244–280, doi:10.1016/0019-1035(89)90038-9.
- Guilbert-Lepoutre, A., J. Lasue, C. Federico, A. Coradini, R. Orosei, and E. D. Rosenberg (2011), 3D thermal evolution model for icy bodies: Application to trans-Neptunian objects, *Astron. Astrophys.*, 529, A71, doi:10.1051/0004-6361/201014194.
- Gulick, V. C. (1998), Magmatic intrusions and a hydrothermal origin for fluvial valleys on Mars, *J. Geophys. Res.*, 103(E8), 19,365–19,387, doi:10.1029/98JE01321.
- Han, L., R. P. Lowell, and C. Lewis (2013), The dynamics of two-phase hydrothermal systems at a seafloor pressure of 25 MPa, *J. Geophys. Res. Solid Earth*, 118, 2635–2647, doi:10.1002/jgrb.50158.
- Hanowski, N. P., and A. J. Brearley (2001), Aqueous alteration of chondrules in the CM carbonaceous chondrite, Allan Hills 81002: Implications for parent body alteration, *Geochim. Cosmochim. Acta*, 65(3), 495–518.
- Hayba, D., and S. Ingebritsen (1994), The computer model Hydrotherm, a three-dimensional finite-difference model to simulate ground-water flow and heat transport in the temperature range of 0 to 1,200 degrees C.
- Helgeson, H., J. Delany, H. Nesbitt, and D. Bird (1978), Summary and critique of the thermodynamic properties of rock-forming minerals, *Am. J. Sci.*, 278, 229.
- Hilairet, N., I. Daniel, and B. Reynard (2006), P–V equations of state and the relative stabilities of serpentine varieties, *Phys. Chem. Miner.*, 33(8–9), 629–637.
- Hirth, G., and S. Guillot (2013), Rheology and tectonic significance of serpentinite, *Elements*, 9(2), 107–113.
- Hirth, G., and D. L. Kohlstedt (1995), Experimental constraints on the dynamics of the partially molten upper mantle: Deformation in the diffusion creep regime, *J. Geophys. Res.*, 100(B2), 1981–2001.
- Horai, K.-I. (1971), Thermal conductivity of rock-forming minerals, *J. Geophys. Res.*, 76(5), 1278–1308, doi:10.1029/JB076i005p01278.
- Hussmann, H., F. Sohl, and T. Spohn (2006), Subsurface oceans and deep interiors of medium-sized outer planet satellites and large trans-Neptunian objects, *Icarus*, 185(1), 258–273, doi:10.1016/j.icarus.2006.06.005.
- Iess, L., R. A. Jacobson, M. Ducci, D. J. Stevenson, J. I. Lunine, J. W. Armstrong, S. W. Asmar, P. Racopappa, N. J. Rappaport, and P. Tortora (2012), The tides of Titan, *Science*, 337(6093), 457–459, doi:10.1126/science.1219631.
- Iess, L., et al. (2014), The gravity field and interior structure of Enceladus, *Science*, 344(6179), 78–80.
- Ingebritsen, S., and M. Appold (2012), The physical hydrogeology of ore deposits, *Econ. Geol.*, 107(4), 559–584.
- Ingebritsen, S., S. Geiger, S. Hurwitz, and T. Driesner (2010), Numerical simulation of magmatic hydrothermal systems, *Rev. Geophys.*, 48, RG1002, doi:10.1029/2009RG000287.
- Jones, G. D., F. F. Whitaker, P. L. Smart, and W. E. Sanford (2004), Numerical analysis of seawater circulation in carbonate platforms: II. The dynamic interaction between geothermal and brine reflux circulation, *Am. J. Sci.*, 304(3), 250–284.
- Karel, J., S. Croft, J. Lunine, and J. Lewis (1991), Rheological properties of ammonia-water liquids and crystal-liquid slurries: Planetary applications, *Icarus*, 89(1), 93–112.
- Kelemen, P. B., and G. Hirth (2012), Reaction-driven cracking during retrograde metamorphism: Olivine hydration and carbonation, *Earth Planet. Sci. Lett.*, 345, 81–89.
- Kelley, D. S., and J. R. Delaney (1987), Two-phase separation and fracturing in mid-ocean ridge gabbros at temperatures greater than 700 C, *Earth Planet. Sci. Lett.*, 83(1), 53–66.
- Kelley, D. S., K. M. Gillis, and G. Thompson (1993), Fluid evolution in submarine magma-hydrothermal systems at the mid-Atlantic ridge, *J. Geophys. Res.*, 98(B11), 19,579–19,596.
- Kenyon, S. J., and B. C. Bromley (2012), Coagulation calculations of icy planet formation at 15–150 AU: A correlation between the maximum radius and the slope of the size distribution for trans-Neptunian objects, *Astron. J.*, 143(3), 63.
- King, T. V., R. Clark, W. Calvin, D. Sherman, and R. Brown (1992), Evidence for ammonium-bearing minerals on Ceres, *Science*, 255(5051), 1551–1553.
- Kohlstedt, D., B. Evans, and S. Mackwell (1995), Strength of the lithosphere: Constraints imposed by laboratory experiments, *J. Geophys. Res.*, 100(B9), 17,587–17,602.

- Korenaga, J., and S.-I. Karato (2008), A new analysis of experimental data on olivine rheology, *J. Geophys. Res.*, **113**, B02403, doi:10.1029/2007JB005100.
- Kumazawa, M., and O. L. Anderson (1969), Elastic moduli, pressure derivatives, and temperature derivatives of single-crystal olivine and single-crystal forsterite, *J. Geophys. Res.*, **74**(25), 5961–5972.
- Küppers, M., et al. (2014), Localized sources of water vapour on the dwarf planet (1) Ceres, *Nature*, **505**(7484), 525–527.
- Lapwood, E. (1948), Convection of a fluid in a porous medium, *Math. Proc. Cambridge Philos. Soc.*, **44**, 508–521.
- Le Ravalec, M., and Y. Guégan (1994), Permeability models for heated saturated igneous rocks, *J. Geophys. Res.*, **99**(B12), 24,251–24,261.
- Li, J.-Y., L. A. McFadden, J. W. Parker, E. F. Young, S. A. Stern, P. C. Thomas, C. T. Russell, and M. V. Sykes (2006), Photometric analysis of 1 Ceres and surface mapping from HST observations, *Icarus*, **182**(1), 143–160.
- Lodders, K. (2003), Solar system abundances and condensation temperatures of the elements, *Astrophys. J.*, **591**, 1220–1247.
- MacDonald, A., and W. Fyfe (1985), Rate of serpentinization in seafloor environments, *Tectonophysics*, **116**(1), 123–135.
- Malamud, U., and D. Prialnik (2013), Modeling serpentinization: Applied to the early evolution of Enceladus and Mimas, *Icarus*, **225**(1), 763–774.
- Malamud, U., and D. Prialnik (2015), Modeling Kuiper belt objects Charon, Orcus and Salacia by means of a new equation of state for porous icy bodies, *Icarus*, **246**, 21, doi:10.1016/j.icarus.2014.02.027.
- Marion, G., J. Kargel, D. Catling, and J. Lunine (2012), Modeling ammonia-ammonium aqueous chemistries in the solar system's icy bodies, *Icarus*, **220**(2), 932–946, doi:10.1016/j.icarus.2012.06.016.
- Martin, J. T., and R. P. Lowell (2000), Precipitation of quartz during high-temperature, fracture-controlled hydrothermal upflow at ocean ridges: Equilibrium versus linear kinetics, *J. Geophys. Res.*, **105**(B1), 869–882.
- Matson, D. L., J. C. Castillo, J. Lunine, and T. V. Johnson (2007), Enceladus' plume: Compositional evidence for a hot interior, *Icarus*, **187**(2), 569–573, doi:10.1016/j.icarus.2006.10.016.
- McCord, T. B., and C. Sotin (2005), Ceres: Evolution and current state, *J. Geophys. Res.*, **110**, E05009, doi:10.1029/2004JE002244.
- McCord, T. B., G. Teeter, G. B. Hansen, M. T. Sieger, and T. M. Orlando (2002), Brines exposed to Europa surface conditions, *J. Geophys. Res.*, **107**(E1), 5004, doi:10.1029/2000JE001453.
- McCord, T. B., J. Castillo-Rogez, and A. Rivkin (2012), Ceres: Its origin, evolution and structure and Dawn's potential contribution, in *The Dawn Mission to Minor Planets 4 Vesta and 1 Ceres*, edited by C. Russell and C. Raymond, pp. 63–76, Springer, New York.
- McKinnon, W. B., and M. E. Zolensky (2003), Sulfate content of Europa's ocean and shell: Evolutionary considerations and some geological and astrobiological implications, *Astrobiology*, **3**(4), 879–897.
- Milliken, R. E., and A. S. Rivkin (2009), Brucite and carbonate assemblages from altered olivine-rich materials on Ceres, *Nat. Geosci.*, **2**(4), 258–261.
- Millington, R. J., and J. P. Quirk (1961), Permeability of porous solids, *Trans. Faraday Soc.*, **57**, 1200–1207.
- Moore, D., D. Lockner, M. Shengli, R. Summers, and J. Byerlee (1997), Strengths of serpentinite gouges at elevated temperatures, *J. Geophys. Res.*, **14**(B7), 14,787–14,801.
- Nestola, F., R. J. Angel, J. Zhao, C. J. Garrido, V. L. Sánchez-Vizcaíno, G. Capitani, and M. Mellini (2010), Antigorite equation of state and anomalous softening at 6 GPa: An in situ single-crystal X-ray diffraction study, *Contrib. Mineral. Petrol.*, **160**(1), 33–43.
- Neveu, M., S. Desch, E. Shock, and C. Glein (2015), Prerequisites for explosive cryovolcanism on dwarf planet-class Kuiper belt objects, *Icarus*, **246**, 48–64, doi:10.1016/j.icarus.2014.03.043.
- Newsom, H. E. (1980), Hydrothermal alteration of impact melt sheets with implications for Mars, *Icarus*, **44**(1), 207–216, doi:10.1016/0019-1035(80)90066-4.
- Norton, D. L. (1984), Theory of hydrothermal systems, *Annu. Rev. Earth Planet. Sci.*, **12**(1), 155–177.
- Norton, D. L., and B. L. Dutrow (2001), Complex behavior of magma-hydrothermal processes: Role of supercritical fluid, *Geochim. Cosmochim. Acta*, **65**(21), 4009–4017.
- Opeil, C., G. Consolmagno, and D. Britt (2010), The thermal conductivity of meteorites: New measurements and analysis, *Icarus*, **208**(1), 449–454.
- Ord, A., B. E. Hobbs, and D. R. Lester (2012), The mechanics of hydrothermal systems: I. Ore systems as chemical reactors, *Ore Geol. Rev.*, **49**, 1–44.
- Osako, M., A. Yoneda, and E. Ito (2010), Thermal diffusivity, thermal conductivity and heat capacity of serpentine (antigorite) under high pressure, *Phys. Earth Planet. Inter.*, **183**(1), 229–233.
- Palguta, J., G. Schubert, and B. Travis (2010), Fluid flow and chemical alteration in carbonaceous chondrite parent bodies, *Earth Planet. Sci. Lett.*, **296**(3), 235–243.
- Paterson, M. S., and T.-F. Wong (2005), *Experimental Rock Deformation—The Brittle Field*, Springer, Berlin.
- Perrillat, J.-P., I. Daniel, K. T. Koga, B. Reynard, H. Cardon, and W. A. Crichton (2005), Kinetics of antigorite dehydration: A real-time X-ray diffraction study, *Earth Planet. Sci. Lett.*, **236**(3), 899–913.
- Person, M., A. Hofstra, D. Sweetkind, W. Stone, D. Cohen, C. Gable, and A. Banerjee (2012), Analytical and numerical models of hydrothermal fluid flow at fault intersections, *Geofluids*, **12**(4), 312–326.
- Phillips, O. M. (1991), *Flow and Reactions in Permeable Rocks*, Cambridge Univ. Press, Cambridge, U. K.
- Pokrovsky, O. S., and J. Schott (1999), Processes at the magnesium-bearing carbonates/solution interface. II. Kinetics and mechanism of magnesite dissolution, *Geochim. Cosmochim. Acta*, **63**(6), 881–897.
- Pokrovsky, O. S., S. V. Golubev, J. Schott, and A. Castillo (2009), Calcite, dolomite and magnesite dissolution kinetics in aqueous solutions at acid to circumneutral pH, 25 to 150 °C and 1 to 55 atm pCO₂: New constraints on CO₂ sequestration in sedimentary basins, *Chem. Geol.*, **265**(1), 20–32.
- Pope, K. O., S. W. Kieffer, and D. E. Ames (2006), Impact melt sheet formation on Mars and its implication for hydrothermal systems and exobiology, *Icarus*, **183**(1), 1–9, doi:10.1016/j.icarus.2006.01.012.
- Prettyman, T., et al. (2011), Dawn's gamma ray and neutron detector, *Space Sci. Rev.*, **163**, 371–459, doi:10.1007/s11214-011-9862-0.
- Rathbun, J. A., and S. W. Squyres (2002), Hydrothermal systems associated with Martian impact craters, *Icarus*, **157**(2), 362–372, doi:10.1006/icar.2002.6838.
- Ribando, R., K. Torrance, and D. Turcotte (1976), Numerical models for hydrothermal circulation in the oceanic crust, *J. Geophys. Res.*, **81**(17), 3007–3012.
- Rimstidt, J. D., and H. Barnes (1980), The kinetics of silica-water reactions, *Geochim. Cosmochim. Acta*, **44**(11), 1683–1699.
- Rivkin, A., E. Volquardsen, and B. Clark (2006), The surface composition of Ceres: Discovery of carbonates and iron-rich clays, *Icarus*, **185**(2), 563–567, doi:10.1016/j.icarus.2006.08.022.
- Rivkin, A., J.-Y. Li, R. Milliken, L. Lim, A. Lovell, B. Schmidt, L. McFadden, and B. Cohen (2011), The surface composition of Ceres, *Space Sci. Rev.*, **163**, 95–116, doi:10.1007/s11214-010-9677-4.

- Robuchon, G., and F. Nimmo (2011), Thermal evolution of Pluto and implications for surface tectonics and a subsurface ocean, *Icarus*, 216(2), 426–439, doi:10.1016/j.icarus.2011.08.015.
- Rousselot, P., E. Jehin, J. Manfroid, O. Mousis, C. Dumas, B. Carry, U. Marboeuf, and J.-M. Zucconi (2011), A search for water vaporization on Ceres, *Astron. J.*, 142, 125.
- Rubin, M. E., S. J. Desch, and M. Neveu (2014), The effect of Rayleigh-Taylor instabilities on the thickness of undifferentiated crust on Kuiper belt objects, *Icarus*, 236, 122–135.
- Russell, C., and C. Raymond (2011), The Dawn mission to Vesta and Ceres, *Space Sci. Rev.*, 163, 3–23, doi:10.1007/s11214-011-9836-2.
- Russell, C. T., et al. (2012), Dawn at Vesta: Testing the protoplanetary paradigm, *Science*, 336(6082), 684–686, doi:10.1126/science.1219381.
- Rutter, E., and K. Brodie (1988), Experimental “syntectonic” dehydration of serpentinite under conditions of controlled pore water pressure, *J. Geophys. Res.*, 93(B5), 4907–4932.
- Safronov, V. (1978), The heating of the Earth during its formation, *Icarus*, 33(1), 3–12.
- Sammis, C., and M. Ashby (1986), The failure of brittle porous solids under compressive stress states, *Acta Metall.*, 34(3), 511–526.
- Schwenzer, S., et al. (2012), Puncturing Mars: How impact craters interact with the Martian cryosphere, *Earth Planet. Sci. Lett.*, 335–336, 9–17, doi:10.1016/j.epsl.2012.04.031.
- Sierks, H., et al. (2011), The Dawn framing camera, *Space Sci. Rev.*, 163(1–4), 263–327.
- Sohl, F., M. Choukroun, J. Kargel, J. Kimura, R. Pappalardo, S. Vance, and M. Zolotov (2010), Subsurface water oceans on icy satellites: Chemical composition and exchange processes, *Space Sci. Rev.*, 153(1–4), 485–510.
- Steele-MacInnis, M., L. Han, R. P. Lowell, J. D. Rimstidt, and R. J. Bodnar (2012), The role of fluid phase immiscibility in quartz dissolution and precipitation in sub-seafloor hydrothermal systems, *Earth Planet. Sci. Lett.*, 321, 139–151.
- Thomas, P., J. W. Parker, L. McFadden, C. T. Russell, S. Stern, M. Sykes, and E. Young (2005), Differentiation of the asteroid Ceres as revealed by its shape, *Nature*, 437(7056), 224–226.
- Thomassin, J., J. Goni, P. Baillif, J. Touray, and M. Jaurand (1977), An XPS study of the dissolution kinetics of chrysotile in 0.1 N oxalic acid at different temperatures, *Phys. Chem. Miner.*, 1(4), 385–398.
- Travis, B., N. Rosenberg, and J. Cuzzi (2003), On the role of widespread subsurface convection in bringing liquid water close to Mars’ surface, *J. Geophys. Res.*, 108(E4), 8040, doi:10.1029/2002JE001877.
- Travis, B., J. Palguta, and G. Schubert (2012), A whole-moon thermal history model of Europa: Impact of hydrothermal circulation and salt transport, *Icarus*, 218(2), 1006–1019, doi:10.1016/j.icarus.2012.02.008.
- Tromans, D., and J. Meech (2002), Fracture toughness and surface energies of minerals: Theoretical estimates for oxides, sulphides, silicates and halides, *Miner. Eng.*, 15(12), 1027–1041.
- Tyburczy, J. A., T. S. Duffy, T. J. Ahrens, and M. A. Lange (1991), Shock wave equation of state of serpentine to 150 GPa: Implications for the occurrence of water in the Earth’s lower mantle, *J. Geophys. Res.*, 96(B11), 18,011–18,027.
- Vance, S., J. Harnmeijer, J. Kimura, H. Hussmann, B. deMartin, and J. M. Brown (2007), Hydrothermal systems in small ocean planets, *Astrobiology*, 7(6), 987–1005, doi:10.1089/ast.2007.0075.
- Voss, C. I., and A. M. Provost (2010), SUTRA—A Model for Saturated-Unsaturated, Variable-Density Ground-Water Flow With Solute or Energy Transport, *U.S. Geol. Surv. Water Res. Invest. Rep.*, 02-4231, 291 pp., Reston, Va.
- Wagner, W., and A. Pruss (2002), The IAPWS formulation 1995 for the thermodynamic properties of ordinary water substance for general and scientific use, *J. Phys. Chem. Ref. Data*, 31(2), 387–536.
- Walsh, J. (1965), The effect of cracks on the compressibility of rock, *J. Geophys. Res.*, 70(2), 381–389.
- Wang, J.-J., J.-G. Zhu, C. Chiu, and H. Zhang (2007), Experimental study on fracture toughness and tensile strength of a clay, *Eng. Geol.*, 94(1), 65–75.
- Weertman, J., S. White, and A. H. Cook (1978), Creep laws for the mantle of the Earth [and discussion], *Philos. Trans. R. Soc. London, Ser. A*, 288(1350), 9–26.
- Xu, T., and K. Pruess (2001), Modeling multiphase non-isothermal fluid flow and reactive geochemical transport in variably saturated fractured rocks: 1. Methodology, *Am. J. Sci.*, 301(1), 16–33.
- Yomogida, K., and T. Matsui (1983), Physical properties of ordinary chondrites, *J. Geophys. Res.*, 88(B11), 9513–9533.
- Young, E. D. (2001), The hydrology of carbonaceous chondrite parent bodies and the evolution of planet progenitors, *Philos. Trans. R. Soc. London, Ser. A*, 359, 2095–2110, doi:10.1098/rsta.2001.0900.
- Young, E. D., K. Zhang, and G. Schubert (2003), Conditions for pore water convection within carbonaceous chondrite parent bodies—Implications for planetesimal size and heat production, *Earth Planet. Sci. Lett.*, 213, 249–259.
- Zolotov, M. Y. (2014), Formation of brucite and cronstedtite-bearing mineral assemblages on Ceres, *Icarus*, 228, 13–26.